Detectability of collective neutrino oscillation signatures in the supernova explosion of a 8.8 $M_\odot$ star

Hirokazu Sasaki,[1,2] Tomoya Takiwaki,[2,*] Shio Kawagoe,[3] Shunsaku Horiuchi,[4,†] and Koji Ishidoshiro[5]

[1]*Department of Astronomy Graduate School of Science, The University of Tokyo, 7-3-1 Hongo, Bunkyo-ku, Tokyo 113-033, Japan*
[2]*Division of Science, National Astronomical Observatory of Japan, 2-21-1 Osawa, Mitaka, Tokyo 181-8588, Japan*
[3]*Institute of Industrial Science, The University of Tokyo, 4-6-1 Komaba, Meguro-ku, Tokyo 153-8505, Japan*
[4]*Center for Neutrino Physics, Department of Physics, Virginia Tech, Blacksburg, Virginia 24061-0435, USA*
[5]*Research Center for Neutrino Science, Tohoku University, Sendai 980-8578, Japan*

(Received 2 July 2019; revised manuscript received 25 November 2019; accepted 19 February 2020; published 26 March 2020)

In order to investigate the impact of collective neutrino oscillations (CNOs) on the neutrino signal from a nearby supernova, we perform three-flavor neutrino oscillation simulations employing the multiangle effect. The background hydrodynamic model is based on the neutrino hydrodynamic simulation of a 8.8 $M_\odot$ progenitor star. We find that CNO commences after some 100 ms post bounce. Before this, CNO is suppressed by matter-induced decoherence. In the inverted mass hierarchy, the spectrum of $\bar{\nu}_e$ becomes softer after the onset of CNO. To evaluate the detectability of this modification, we define a hardness ratio between the number of high energy neutrino events and low energy neutrino events adopting a fixed critical energy. We show that Hyper-Kamiokande (HK) can distinguish the effect of CNO for supernova distances out to ∼10 kpc. On the other hand, for the normal mass hierarchy, the spectrum of ν_e becomes softer after the onset of CNO, and we show that DUNE can distinguish this feature for supernova distances out to ∼10 kpc. More work is necessary to optimize the best value of critical energy for maximum sensitivity. We also show that if the spectrum of $\bar{\nu}_e$ in HK becomes softer due to CNO, the spectrum of ν_e in DUNE becomes harder, and vice versa. These synergistic observations in $\bar{\nu}_e$ and ν_e, by HK and DUNE, respectively, will be an intriguing opportunity to test the occurrence of CNO.

DOI: 10.1103/PhysRevD.101.063027

I. INTRODUCTION

A major goal of low-energy neutrino astronomy is observing a high statistics neutrino signal from a nearby core-collapse supernova [1]. The neutrino burst from SN1987A was an epoch-making observation that demonstrated the crucial link that massive stars release huge amounts of energy at their endpoints in the form of neutrinos and trigger a supernova explosion. Even with limited neutrino event statistics (about 20 events), the signal revealed much about the importance of weak-interaction physics in the core collapse. Tens of thousands of neutrino events are expected from the next nearby core-collapse supernova, and the events are anticipated to provide unprecedented information about the explosion (see, e.g., the reviews [2–9]).

There are multiple operational neutrino observatories that can detect a high-statistics neutrino burst event from a nearby supernova, e.g., Super-Kamiokande (SK) [10], IceCube [11–13], and KamLAND [14]. SK is able to obtain both the light curve and spectrum of the neutrino. To decrease the background using a coincident tagging technique, SK will soon be upgraded with gadolinium [15]. IceCube plays an important role in detecting time variability of the signal with high statistics, by taking advantage of its large volume [16]. KamLAND is sensitive to low-energy neutrinos and is even sensitive to neutrinos emitted during the last Si-burning phase of the progenitor [14]. In the future, large volume detectors such as Hyper-Kamiokande (HK) [17] and JUNO [18] will become available for detecting electron antineutrinos out to further distances, while DUNE [19] will dramatically enhance the capabilities to detect electron neutrinos.

In parallel to the development of neutrino observation facilities, the theory of neutrino emission and their propagation through the supernova and progenitor have dramatically progressed [2,3,6]. The technique of neutrino radiation hydrodynamics has become highly sophisticated [20–26] and can provide reliable neutrino luminosities

*takiwaki.tomoya.astro@gmail.com
†horiuchi@vt.edu

 © 2020 American Physical Society

and average energies. Using reliable techniques, three-dimensional simulations are now available [27–34], and many interesting phenomena have been discovered, e.g., SASI [31,35], LESA [36], and low-$T/|W|$ instability [37].

Perhaps the most distinct progress in the theory of neutrino propagation is the realization that collective neutrino oscillations (CNO) can operate in the supernova environment (see, e.g., reviews [38] and references therein). CNO is an oscillation that happens in the high density region of neutrinos and leads to a potential for the flavor oscillation. In this sense, CNO is similar to the Mikheyev-Smirnov-Wolfenstein (MSW) effect [39,40]; however, the effect of CNO is complicated since the potential is made by the neutrinos themselves and makes the problem nonlinear. Interesting features of the oscillated neutrino energy spectra, caused by so-called spectral swaps, have been obtained by pioneering CNO studies [41–43]. To predict the spectra, Duan *et al.* (2006) formulated the basic quantities and oscillation modes [42]. Fogli *et al.* (2009) argued that spectral splits emerge as dominant features in the inverted mass hierarchy [43]. Note that the value of θ_{13} was not known very well at the time of these studies [44].

Although initial works on CNO assumed generic matter and neutrino profiles, recent works employ the results of numerical simulation of neutrino radiation hydrodynamics [45–51]. One important finding in these works is the importance of matter-induced decoherence, so-called matter suppression [45,46,48,52,53]. Essentially, if the matter density is higher than the neutrino density, the wavelength of the neutrino's wave function becomes short, and the different paths from the protoneutron star cause significant decoherence of the wave functions. As a result, CNO is highly suppressed in such epochs. After this finding, extensive studies of CNO were provided by Wu *et al.* (2015), where a progenitor of 18.0 $M_\odot$ was used [50]. The rates of neutrino events expected at SK and DUNE were computed, and the possibility to distinguish the neutrino mass hierarchy has been suggested.

One important lesson from previous studies is that the final neutrino spectrum is significantly affected by not only the neutrino fluxes but also average energies and angular distributions. Recently, Horowitz *et al.* (2017) proposed a new reaction rate of neutrino nucleon scattering [54]. This causes the neutrino flux to significantly change, potentially impacting previous CNO results [50].

In this paper, we investigate the impact of CNO on the neutrino events from a nearby supernova and discuss its detectability. We perform the first such study using the set of new neutrino reaction rates of Horowitz *et al.* (2017) and Horowitz (2002) [54,55], as well as the other new reaction rates that are summarized in Ref. [56]. These new reactions can change the neutrino emission and hence the resulting neutrino oscillation and detection. The structure of the paper is as follows. In Sec. II, we introduce our numerical schemes for the hydrodynamic simulations and the neutrino oscillation computations. In Sec. III, we discuss our results, starting with the dynamics of the explosion, followed by features of neutrino oscillations and, finally, the detectability of CNO. In Sec. IV, we summarize our results.

II. METHODS

We performed two kinds of numerical simulations. The first one is the hydrodynamic simulation of core-collapse supernova from a progenitor model. The second one is that for the three-flavor neutrino oscillations using snapshots obtained by the hydrodynamic simulation. In this section, we explain the numerical methods and settings for each.

The hydrodynamic simulation was performed by the 3DnSNe code (see Refs. [29,52,56–60] for recent application of this code). The evolution of the variables is solved in the coordinates of spherical polar geometry. A piecewise linear method with the geometrical correction is used to reconstruct variables at the cell edge, where a modified van Leer limiter is employed to satisfy the condition of total variation diminishing (TVD) [61]. The numerical flux is calculated using the HLLC solver [62]. The models are computed on a one-dimensional spherical polar coordinate grid with a resolution of 512 radial zones. The radial grid is logarithmically spaced and covers from the center up to the outer boundary of 5000 km. Recently, we updated our neutrino reactions [56]. Among them, the effect of virial expansion on the neutrino nucleon scattering is important, and this significantly changes the neutrino flux [54]. The equation of state used in the simulation is the Lattimer and Swesty one with incomprehensibility of $K = 220$ MeV [63]. Although the code employs the relatively simple neutrino transport scheme of the isotropic diffusion source approximation (IDSA) [64], it nevertheless can provide consistent results on neutrino luminosities and average energies with more sophisticated schemes (see Ref. [57] for a detailed comparison).

The progenitor employed in this study is an 8.8 $M_\odot$ star [65–67]. The setup of the envelope is the same as that of Kitaura *et al.* (2006) [68]. Since the density of the envelope is low in this model, the matter suppression is weak and the signature of the CNO is expected. In the context of neutrino oscillations, Saviano *et al.* (2012) also use this progenitor [48].

Flavor transitions of free-streaming neutrinos are calculated as postprocesses of the hydrodynamic simulation whose time snapshots give us the strength of the electron matter potential [39,40] and that of the neutrino self-interaction [42,50,52,53,69–74]. Neutrino oscillation parameters in our simulation are given by the following values: $\sin^2(2\theta_{12}) = 0.84$, $\sin^2(2\theta_{23}) = 1$, $\sin^2(2\theta_{13}) = 0.19$, $\Delta m^2_{21} = 7.9 \times 10^{-5}$ eV^2, $|\Delta m^2_{32}| = 2.0 \times 10^{-3}$ eV^2, and $\delta_{\rm CP} = 0$ where $\Delta m^2_{ij} = m^2_i - m^2_j$. We employ the bulb model [42] and solve the time evolution of the neutrino

and antineutrino density matrices in three-flavor multiangle calculations based on Ref. [52].

We sample 50 points in neutrino energy $E \leq 60$ MeV and choose 1000 neutrino angular modes, which are typical values to prevent numerical multiangle decoherence [75]. The radius of the neutrinosphere is fixed at 30 km, which is close to sharp declines in the baryon density profiles. In reality, the position of the neutrinosphere depends on the neutrino energy and flavor. In the bulb model, however, multiple neutrinospheres cannot be employed. This is one of the major caveats of this study. The results of adopting a different neutrinosphere radius are shown in the Appendix A.

The spectra of supernova neutrinos often show pinched shapes [31,76] compared to nondegenerate Fermi-Dirac distributions. To capture this feature, we set the initial neutrino spectra on the surface of the neutrinosphere, $\phi_i(E)(i = \nu_e, \bar{\nu}_e, \nu_X)$, as a Gamma distribution,

$$\phi_i(E) = \Phi_i^0 \frac{E^{\alpha_i}}{\Gamma_{\alpha_i+1}} \left(\frac{\alpha_i + 1}{\langle E_i \rangle}\right)^{\alpha_i+1} \exp\left[-\frac{(\alpha_i + 1)E}{\langle E_i \rangle}\right], \quad (1)$$

whose pinching parameter, $\alpha_i = \frac{\langle E_i^2 \rangle - 2\langle E_i \rangle^2}{\langle E_i \rangle^2 - \langle E_i^2 \rangle}$, is estimated from the neutrino mean average energies $\langle E_i \rangle$ and rms average energies $\sqrt{\langle E_i^2 \rangle}$. These parameters, as well as the number luminosity Φ_i^0, are derived from the result of the neutrino radiation hydrodynamic simulation (see Sec. III A and the middle panel of Fig. 2). The multiangle calculations are carried out up to 1500 km, where CNOs have finished. In our simulation, MSW resonances do not appear in neutrino energy $E \geq 3$ MeV within 1500 km because of the high electron number density.

III. RESULTS

We discuss the impact of neutrino oscillations on the detection rates at the observation facilities HK, JUNO, and DUNE. We first introduce our hydrodynamic setups. In particular, the radial profile of the density and electron fraction, as well as neutrino luminosity and energies, are employed from the hydrodynamic simulation. Then, we introduce our calculation of neutrino oscillations, followed by detection.

A. Hydrodynamic model

The dynamics of the supernova explosion is characterized by the shock. In our model, the shock is revived quite early by neutrino heating. The black curve of Fig. 1 shows the evolution of the averaged shock radius. The shock revival time is 90 ms after bounce. We adopt the widely used convention of shock revival time defined as the time when the shock reaches 400 km [77]. This early shock revival time is due to the low mass accretion rates of this progenitor, which has a very diluted envelop (see Fig. 2 of Ref. [78]). After shock revival, the shock continuously expands and reaches 1000 km at 120 ms after bounce. This result agrees with previous works (e.g., Fig. 3 of Ref. [79]). It should be noted that shock revival happens even in 1D geometry for this progenitor.

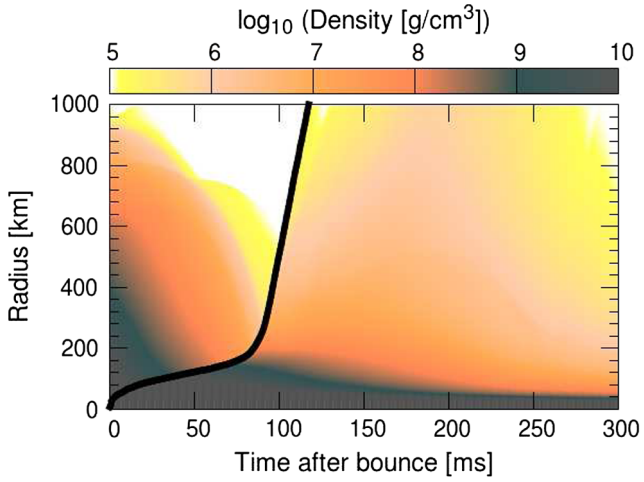

FIG. 1. The black curve is the time evolution of the shock radius. The colored areas show the time evolution of the logarithmic density profile [g/cm^3]. The horizontal axis is the time after bounce in ms, and the vertical axis shows the radial coordinates in km.

After shock revival, the density of the shocked region decreases. The color map of Fig. 1 shows the logarithmic density as a function of time and radius. As shown later, the region above 200 km is important for the neutrino oscillation in this model. Before 50 ms postbounce, the density in the region is high and exceeds 10^9 g/cm^3. During this phase, the density gradually decreases with time due to the decrease of the mass accretion rate. After the shock revival around 90 ms postbounce, the density briefly increases as a function of time since mass is ejected from the central region. During this epoch, the density reaches $\sim 10^{7-8}$ g/cm^3 at ~180 ms postbounce. However, after this, the density decreases due to the decrease of mass ejection from the central region. In the calculation of neutrino oscillations, we select several time snapshots and use the profiles of the density Y_e at the corresponding times.

The information of the neutrino spectra is necessary for the input of the simulation of CNO. The evolutions of the neutrino luminosities and energies are shown in Fig. 2. The green, red, and blue curves correspond to ν_e, $\bar{\nu}_e$, and ν_X, respectively.

In the top panel, the luminosities after 150 ms postbounce do not deviate much from those of Ref. [46]. Before 150 ms, our luminosities are higher than those of Ref. [46] since an updated set of neutrino opacities is used (see Fig. 15 of Ref. [56]). In our model, the luminosity of an antielectron neutrino is larger than that of an electron-type neutrino. This feature is not prominent in previous works

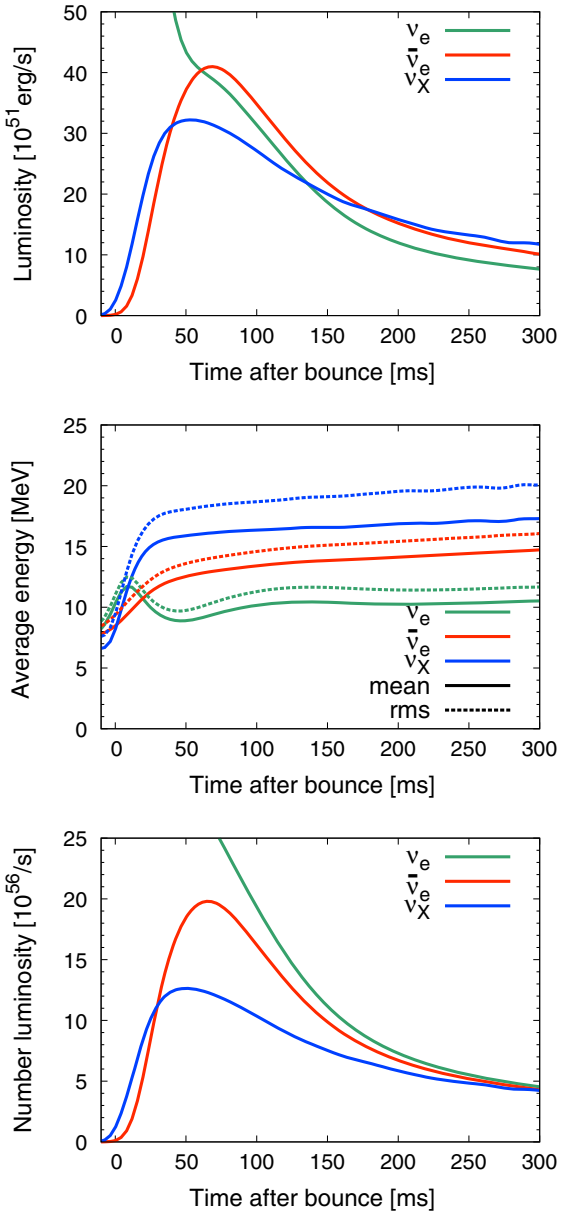

FIG. 2. Time evolution of the neutrino luminosity (top panel), the neutrino average energy (central panel), and the neutrino number luminosity (bottom panel). In all panels, the green, red, and blue curves correspond to ν_e, $\bar{\nu}_e$, and ν_X, respectively. In the middle panel, the solid line denotes the mean energy, and the dotted line is the rms energy. We evaluate the luminosities and energies at 500 km and assume the bulb model; i.e., those luminosities and energies are set to the neutrinosphere in the oscillation simulations.

(see Fig. 1 of Ref. [46] and the hydrodynamic model of Ref. [80] for the details of the setting). Our feature may originate from the employment of weak magnetism [55], which is not used in previous works. The weak magnetism decreases the opacity for the antielectron neutrino, making them easier to escape. This would enlarge the antineutrino luminosity.

In the middle panel, the hierarchy of the average energy is consistent with other simulations during the accretion phase: $\nu_X > \bar{\nu}_e > \nu_e$. The average is also higher compared to that of Ref. [46] due to the new reaction set (see Fig. 15 of Ref [56] again). The hierarchy of the number luminosity has an interesting feature.

In the bottom panel, the number luminosity is shown, and initially the hierarchy is $\nu_X < \bar{\nu}_e < \nu_e$, which is typical in the accretion phase of core-collapse supernovae. However, at 300 ms postbounce, all number luminosities converge, and there is no hierarchy. This feature leads to interesting flavor mixing as discussed later.

B. Neutrino oscillation

Using snapshots taken from the hydrodynamic simulation, we calculate the neutrino oscillation. We use the rotated frame of $e-x-y$ instead of the flavor frame of $e-\mu-\tau$ [81]. In this section, we mainly focus on oscillations. The application to detection is discussed in the next section.

1. Appearance of CNO

The appearance of CNO is strongly affected by the density profile. In our models, CNO appears before 100 ms postbounce. In Fig. 3, the survival probability after CNO is shown as a function of the neutrino energy. The top panel is for the inverted mass hierarchy. At 31 ms postbounce, the survival probability is almost 1.0, and CNO is suppressed by the dense matter above the shock wave (the radius is above ~200 km). At 81 ms postbounce, the density in the region becomes smaller, and the survival probability becomes 0.2 for most of the energy range except a narrow range of a few MeV. The appearance of CNO in such an early epoch is due to our choice of the progenitor. The 8.8 $M_\odot$ star has an extraordinary dilute envelop among the progenitors of core-collapse supernovae (see Fig. 1 of Ref. [79]). At 181 ms, the density of the region becomes slightly higher due to the shocked matter arising from the center. At this point, the survival probability becomes 1.0 due to matter suppression but only for neutrino energies below 10 MeV. The time of the occurrence of CNO also depends on the neutrino spectral shape. If the spectral shape is more like a Fermi-Dirac distribution, the onset time is significantly delayed and becomes 231 ms (see Fig. 15 in Appendix B).

The survival probability in the case of the normal mass hierarchy is roughly similar to that of the inverted mass hierarchy but generally more suppressed. The bottom panel of Fig. 3 shows the evolution as a function of neutrino energy and time. Like in the inverted mass hierarchy, the appearance of CNO occurs before 100 ms. However, at 181 ms postbounce, the CNO is suppressed due to the increase in the matter density over all neutrino energies (see the density evolution at ~200 km in Fig. 1). Though the suppression also appears in the inverted mass hierarchy, it is

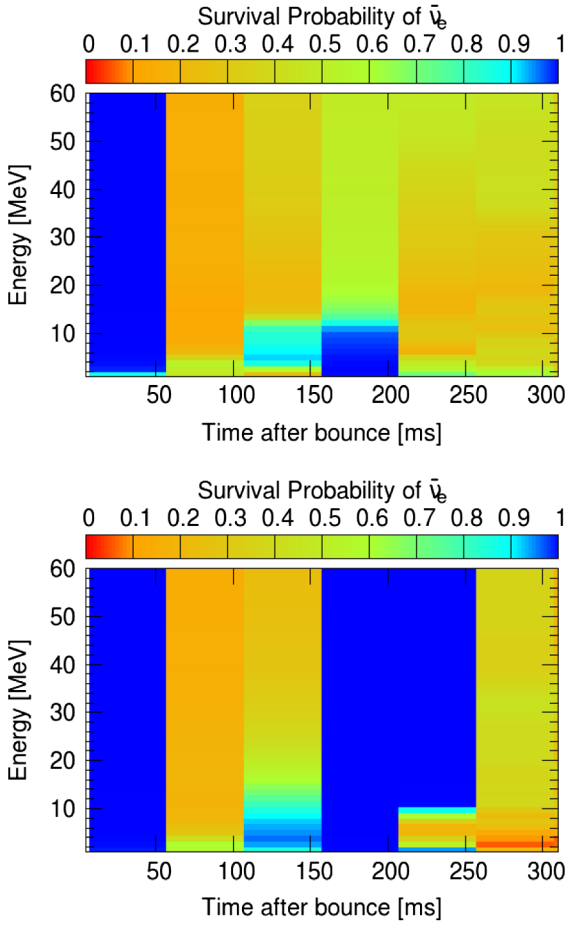

FIG. 3. The survival probabilities of an electron antineutrino at a radius of 1500 km as a function of neutrino energy and emission time. Top panel: The probability for the inverted mass hierarchy. Bottom panel: The probability for the normal mass hierarchy. In both panels, we employ the multiangle method to calculate neutrino oscillations, and the Gamma function [Eq. (1)] is used for the neutrino spectrum.

stronger in the normal mass hierarchy case. A strong suppression is also seen in the Fermi-Dirac neutrino spectrum (see Fig. 15 in Appendix B), where it can be seen that the appearance of CNO is delayed to 281 ms, which is later than in the inverted mass hierarchy, 231 ms.

2. Neutrino oscillation in the inverted mass hierarchy

The radial profiles of conversion probabilities $P_{e\alpha} = P(\bar{\nu}_e \to \bar{\nu}_\alpha)(\alpha = e, x, y)$ [71] are helpful to understand the behavior of nonlinear flavor transitions. In Fig. 4, we present the conversion probabilities of antineutrinos at 231 ms in the inverted mass hierarchy. Such probabilities are derived from angle-averaged diagonal components of density matrices [see Eq. (11) in Ref. [52]]. The top panel corresponds to the evolution of the survival probabilities of $\bar{\nu}_e$. The value of P_{ee} remains unity as long as flavor transitions are negligible. The middle and bottom panels show how emitted $\bar{\nu}_e$ on the surface of the neutrinosphere is

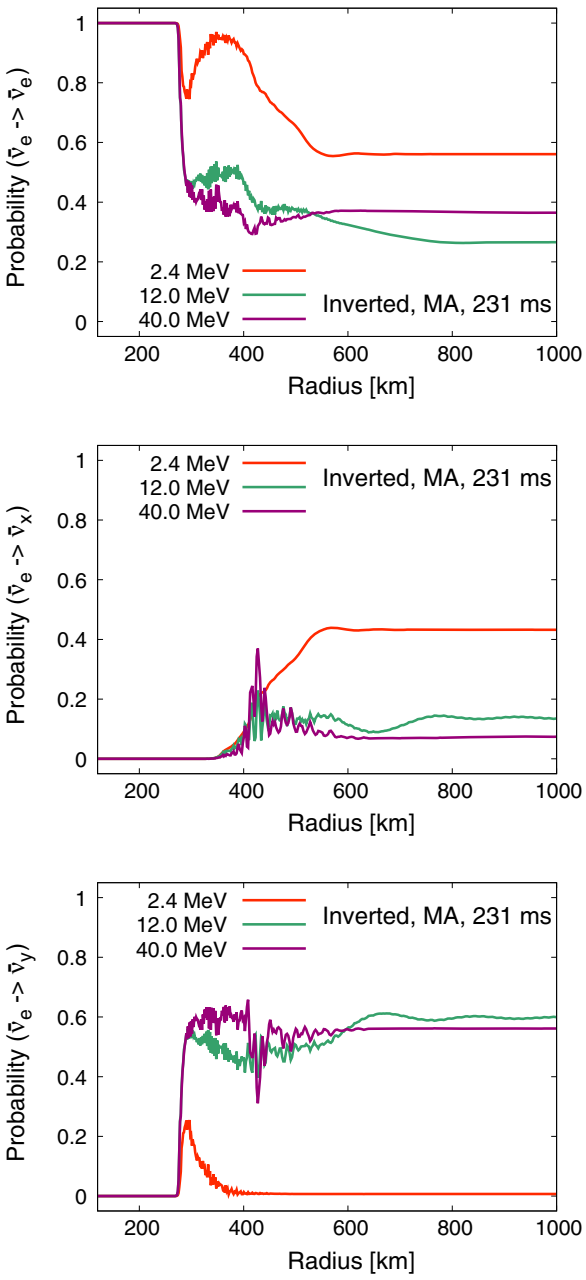

FIG. 4. The radial profiles of conversion probabilities of $\bar{\nu}_e$ at 231 ms postbounce. The inverted mass hierarchy is assumed, and the multiangle scheme (labeled MA) is used. The different colors show the profile at different energies of the neutrino: Red, green, and violet correspond to 2.4, 12.0, and 40.0 MeV, respectively.

transformed to $\bar{\nu}_y$ and $\bar{\nu}_x$, respectively. We solve the time evolution of neutrino and antineutrino density matrices in three-flavor multiangle calculations. Nondiagonal components in neutrino self-interaction Hamiltonians increase prominently when self-interaction terms couple with the vacuum Hamiltonian. Such a nondiagonal potential gives rise to nonlinear collective motion in flavor space.

As expected, the electron antineutrinos essentially experience CNO in the $e - y$ sector in the inverted mass

hierarchy. In Fig. 4, we show the flavor evolution in the inverted mass hierarchy for three $\bar{\nu}_e$ energies: 2.4 MeV, 12.0 MeV, and 40.0 MeV. It can be seen that CNO starts at around 250 km in the $e-y$ sector; the survival probability decreases (top panel), and the conversion probability for $e-y$ becomes larger (bottom panel), except for the low energy component of 2.4 MeV.

Subsequent CNO occurs in $\bar{\nu}_x$ at 450 km after the early $e-y$ mixing. Two types of nonlinear transitions reflect the coupling of self-interactions with two vacuum frequencies, $\omega_{\rm solar} = \Delta m^2_{21}/2E$ and $\omega_{\rm atm} = |\Delta m^2_{32}|/2E$. Such three-flavor peculiar mixing was also found in previous numerical studies [71,72], and it arises from a small flavor asymmetry in the neutrino number luminosity, e.g., at 231 ms: $\Phi^0_{\nu_e} : \Phi^0_{\bar{\nu}_e} : \Phi^0_{\nu_x} = 1.17 : 1.09 : 1.00$. As shown in the bottom panel of Fig. 2, the flavor asymmetry becomes smaller as time proceeds, which enhances the three-flavor mixing in the postaccretion phase. At 600 km, CNO has finished, and conversion probabilities settle down to constant values. Then, final flavor mixing is energy dependent. For example, low energy electron antineutrinos actively transform to other flavor $\bar{\nu}_x$, and $\bar{\nu}_y$ returns to the original flux as shown by the 2.4 MeV curves in Fig. 4. On the other hand, $e-x$ mixings become small in more energetic electron antineutrinos, for example, 12.0 and 40.0 MeV, even though the vacuum frequency $\omega_{\rm atm}$ induces partial $\bar{\nu}_y - \bar{\nu}_x$ conversions.

The top panel of Fig. 5 shows the spectrum of antineutrinos at 231 ms postbounce after the CNO (i.e., at 1500 km, in red), compared to the original $\bar{\nu}_e$ (green) and ν_X (blue). This $\bar{\nu}_e$ spectrum traces the property of survival probabilities in the top panel of Fig. 4. In the high energy range, $E > 12$ MeV, a spectral oscillation occurs actively in the $e-y$ sector. The $e-x$ conversion is suppressed. Complete spectral swaps, which are generally observed under the single-angle approximation [42], fail in multi-angle simulations because the coherence of nonlinear flavor transitions are smeared out by angular dispersion in the matter potential [82]. In the region of $E < 12$ MeV, the spectrum is rather close to the original spectrum, and interestingly the $e-x$ conversion is dominant. In general, three-flavor mixing would induce complex spectral swaps in the outer layers, different from a simple two-flavor picture. However, the low energy events do not strongly contribute to the total event rates.

3. *Neutrino oscillation in the normal mass hierarchy*

In the case of normal mass hierarchy, CNO appears in two typical time domains, ∼100 ms and ∼300 ms postbounce, while it is suppressed around ∼200 ms. In the case of inverted mass hierarchy, CNO continues after 50 ms after bounce. Such hierarchy differences may come from the multiangle suppression [72] of the $e-x$ and $e-y$ sectors.

At ∼100 ms, the $e-x$ conversion occurs dominantly in the normal mass hierarchy. The role of $\bar{\nu}_x$ in the normal

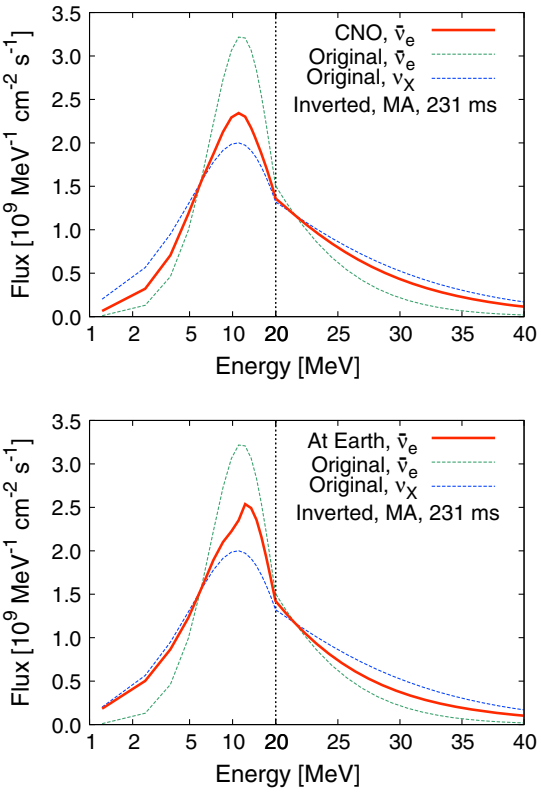

FIG. 5. Flux spectra of electron antineutrinos in the inverted mass hierarchy (red solid line). For comparison, the original electron neutrino (green dotted line) and heavy lepton neutrino (blue dotted line) are shown. The time snapshot of 231 ms is used. Top panel: CNO with the MA scheme (1500 km from the center; note that the vertical axis has been rescaled to a source distance of 10 kpc). Bottom panel: Flux spectrum at the Earth, including all oscillation effects (CNO, MSW, vacuum). Note that in both panels, the horizontal axis is logarithmic for $E < 20$ MeV and linear for $E > 20$ MeV in the both panels (indicated by the vertical dashed line).

mass hierarchy is that of $\bar{\nu}_y$ in the inverted mass hierarchy. In the inverted mass hierarchy, the $e-y$ conversion occurs dominantly thorough almost all energy regions, and only in the low energy region, $e-x$ conversion can happen. This feature is clearly seen in Fig. 6. The survival probabilities of 12.0 MeV and 40.0 MeV tend to about 0.2, while the survival probability of low energy neutrinos (2.4 MeV) is about 0.5 at 1500 km. A significant fraction of electron antineutrinos are converted to x antineutrinos. CNO takes place before the MSW resonances because the matter potential, $\lambda_r = \sqrt{2} G_{\rm F} n_e$, is higher than the atmospheric vacuum frequency $\omega_{\rm atm}$ around the onset of CNO, ∼700 km. The λ_r and $\omega_{\rm atm}$ are shown in Fig. 7. The upper band of $\omega_{\rm atm}$ comes from that of the lowest energy, 1.2 MeV. The low energy neutrino ($E < 3$ MeV) enters the region of MSW effects before the outer boundary of 1500 km. Since the low energy neutrino does not strongly affect the observational signal, we do not focus on this effect.

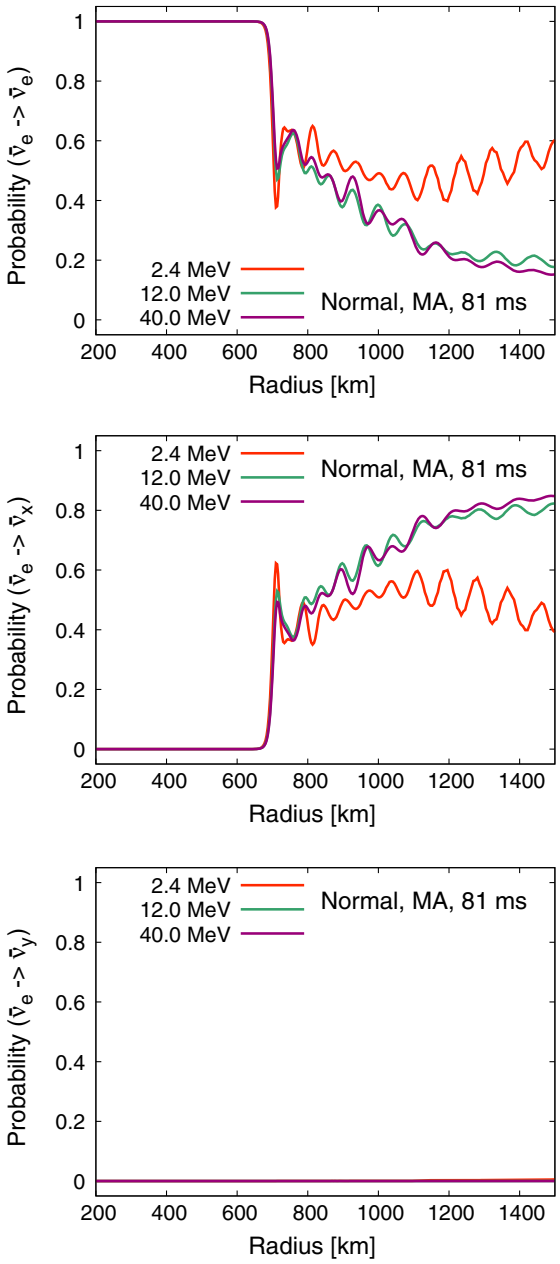

FIG. 6. The radial profiles of conversion probabilities of $\bar{\nu}_e$ at 81 ms postbounce. The normal mass hierarchy is assumed, and the multiangle scheme (labeled MA) is used. The different colors show the profile at different energies of the neutrino: Red, green, and violet correspond to 2.4, 12.0, and 40.0 MeV, respectively.

At ∼200 ms, the matter follows the expanding shock, and the density above 200 km becomes higher. CNO ceases at that time by strong matter suppression.

At ∼300 ms, CNO again occurs because the electron density becomes lower outside the neutrinosphere. The three-flavor mixing is significant due to the small asymmetry between neutrino number luminosities [72]. We find that several types of CNO contribute in different radii: $e-y$ mixing ($r < 270$ km), $e-x$ mixing ($r > 270$ km), and $x-y$ mixing ($r > 340$ km) in high energy neutrinos and

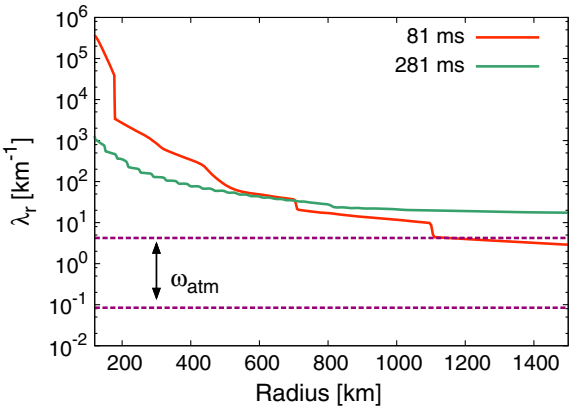

FIG. 7. The time snapshots of matter potential $\lambda_r = \sqrt{2}G_F n_e$ for 81 and 281 ms postbounce. The horizontal band shows the values of atmospheric vacuum frequencies $\omega_{atm} = |\Delta m^2_{32}|/2E$ for $E[\mathrm{MeV}] \in [1.2, 60]$. The upper line corresponds to that of the lowest energy. The MSW resonance occurs when the matter potential enters the band of ω_{atm}.

antineutrinos. For example, such three-flavor mixing of 40 MeV antineutrinos at 281 ms is shown in Fig. 8. The small amount of $e-y$ conversion starts around 150 km, which comes from the coupling of neutrino self-interactions with ω_{atm}. After that, the significant $e-x$ conversion occurs around 270 km in this later explosion phase. Then, a subsequent $x-y$ conversion around 340 km increases the three-flavor mixing in high energy antineutrinos. Such flavor conversion is also confirmed in neutrinos. It seems that, in the normal mass hierarchy, the $e-x$ conversion becomes the main process of CNO in high energy neutrinos and antineutrinos across the examined time window, irrespective of the three-flavor mixing in the later explosion phase. Figure 7 indicates that the origin of the $e-x$ conversion in the normal mass

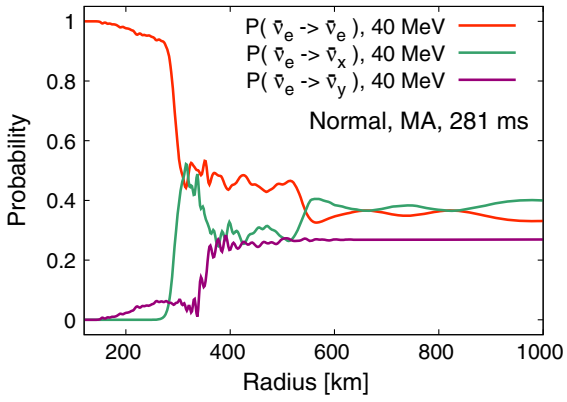

FIG. 8. The radial profiles of conversion probabilities of electron antineutrinos at 281 ms postbounce in the normal mass hierarchy. The different colors show the profiles of different conversion probabilities of $\bar{\nu}_e$: $P_{e\alpha} = P(\bar{\nu}_e \to \bar{\nu}_\alpha)(\alpha = e, x, y)$ whose energy is 40 MeV. The red, green, and violet lines correspond to P_{ee}, P_{ex}, and P_{ey}, respectively.

hierarchy does not come from a "MSW prepared spectral split" as confirmed in the neutronization neutrino burst [83–85] because the value of λ_r does not reach that of $\omega_{\rm atm}$ at the onset of the $e-x$ conversion, ~270 km (see the green curve of Fig. 7).

The significant $e-x$ conversion in the normal mass hierarchy has not been shown by previous three-flavor simulations [71,72,81]. We discuss a possible mechanism of such a new type of flavor mixing, which would be equivalent to an instability for normal mass hierarchy suggested in a recent work [86]. We begin with a simpler problem. Namely, in two-flavor collective neutrino oscillations, the relation between the direction of the vacuum polarization vector $\omega\mathbf{B}$ and the nonlinear polarization vector $\mathbf{D}$ is crucial for the development of nonlinear effects [87]. Here, the direction of the polarization vector $\mathbf{P}=(P_x,P_y,P_z)$ is given by the sign of the z component (note in this discussion the meanings of x, y are different from that of the rotated basis). The initial value of the nonlinear potential is independent of neutrino mass hierarchy, so we only focus on the z component of the vacuum polarization vector in each neutrino sector. Now, in reality, we have to consider three-flavor cases. In the rotated basis (ν_e,ν_x,ν_y), the vacuum Hamiltonian of three-flavor neutrinos [52] is described by

$$\Omega(E)=\frac{\Delta m^2_{21}}{6E}\begin{pmatrix}1-3c^2_{12}c^2_{13} & 3c_{12}s_{12}c_{13} & 3c^2_{12}s_{13}c_{13}\\ 3c_{12}s_{12}c_{13} & 1-3s^2_{12} & -3s_{12}c_{12}s_{13}\\ 3c^2_{12}s_{13}c_{13} & -3s_{12}c_{12}s_{13} & 1-3c^2_{12}s^2_{13}\end{pmatrix}+\frac{\Delta m^2_{32}}{6E}\begin{pmatrix}-1+3s^2_{13} & 0 & 3s_{13}c_{13}\\ 0 & -1 & 0\\ 3s_{13}c_{13} & 0 & -1+3c^2_{13}\end{pmatrix}, \tag{2}$$

where c_{ij} and s_{ij} stand for $\cos\theta_{ij}$ and $\sin\theta_{ij}$, respectively. This three-flavor vacuum Hamiltonian is equivalent to Eq. (6) in Ref. [81] even though we employ different normalization: $\mathrm{Tr}\Omega(E)=0$. The nonlinear potential of neutrino self-interactions first couples to the second term on the right-hand side of Eq. (2) because $|\Delta m^2_{32}|/\Delta m^2_{21}>O(10)$. From the definition of polarization (Bloch) vectors in a 2×2 Hermite matrix [69], the z component of the vacuum Hamiltonian in the $e-y$ sector is obtained by the difference between two diagonal components in the $e-y$ sector,

$$\Omega(E)_{ee}-\Omega(E)_{yy}\sim-\frac{\Delta m^2_{32}}{2E}\cos 2\theta_{13}, \tag{3}$$

where the sign of Δm^2_{32} depends on the neutrino mass hierarchy. If the sign of D_z is positive, $\Phi^0_{\nu_e}>\Phi^0_{\bar\nu_e}$, the positive sign in Eq. (3) is preferable for significant flavor transitions in the $e-y$ sector, as shown in two-flavor CNO in the inverted mass hierarchy ($\Delta m^2_{32}<0$) [42,69].

We remark that some $e-y$ conversion also appears even in the normal mass hierarchy (e.g., the slight increase of P_{ey} within 270 km in Fig. 8) if the asymmetry among neutrino number luminosities $\Phi^0_i(i=\nu_e,\bar\nu_e,\nu_x)$ is small enough to induce multiple spectral swaps in the inverted mass hierarchy [71]. In our explosion model, the asymmetry of neutrino number luminosity gradually decreases as shown in the bottom panel of Fig. 2. The $e-x$ conversions in the normal mass hierarchy can be discussed in the same way as $e-y$ conversions above. Large instabilities would appear in $e-x$ conversions if the z component of the vacuum Hamiltonian in the $e-x$ sector,

$$\Omega(E)_{ee}-\Omega(E)_{xx}=-\frac{\Delta m^2_{21}}{2E}(\cos 2\theta_{12}-\cos^2\theta_{12}\sin^2\theta_{13})+\frac{\Delta m^2_{32}}{2E}\sin^2\theta_{13}, \tag{4}$$

takes positive values. In the inverted mass hierarchy ($\Delta m^2_{32}<0$), the sign of Eq. (4) is always negative because $\Delta m^2_{21}>0$ and $|\Delta m^2_{32}|/\Delta m^2_{21}>O(10)$. However, Eq. (4) becomes positive in the normal mass hierarchy ($\Delta m^2_{32}>0$) if we impose a finite mixing angle θ_{13} larger than below a critical value

$$\sin^2\theta_{13}>\frac{\cos 2\theta_{12}}{\Delta m^2_{32}/\Delta m^2_{21}+\cos^2\theta_{12}}. \tag{5}$$

This condition may also be applicable in a dense electron background before MSW resonances because diagonal terms in the matter potential can be canceled out in a corotating frame [42], which moves together with the nonlinear potential of neutrino self-interactions. Therefore, the above criterion may be applicable to a sparse electron background. Our neutrino mixing parameters satisfy the above condition. This is also true for more updated values of neutrino mixing parameters [88]. On the other hand, Eq. (5) is violated in the case of the small mixing angle θ_{13} used in previous studies [71,72,81]. This seems to be a plausible reason why the $e-x$ conversions in the normal mass hierarchy are discovered in our simulation but not confirmed in Refs. [71,72,81]. As shown in the bottom panel of Fig. 3, flavor conversions in the normal mass hierarchy are easily suppressed in a dense electron background. Therefore, the $e-x$ conversions in the normal mass hierarchy would be fragile in more massive progenitor models. Nevertheless, further studies are necessary for more robust conclusions.

C. Detectability of the feature of CNO

Next we discuss the detectability of the signatures of CNO. The neutrino flux at the Earth, $f^{(\rm f)}_\nu$, can be estimated by Eqs. (23) and (24) of Ref. [50]. In these equations, the effect of MSW is included, and that of the Earth is not included. The rotated frame of $e-x-y$ is also used [81].

For convenience, we summarize the relevant parts. For normal mass hierarchy, the equations are

$$f_{\nu_e}^{(\mathrm{f})} = s_{13}^2 f_{\nu_e}^{(\mathrm{a})} + c_{12}^2 c_{13}^2 f_{\nu_x}^{(\mathrm{a})} + s_{12}^2 c_{13}^2 f_{\nu_y}^{(\mathrm{a})}, \tag{6}$$

$$f_{\bar{\nu}_e}^{(\mathrm{f})} = c_{12}^2 c_{13}^2 f_{\bar{\nu}_e}^{(\mathrm{a})} + s_{12}^2 c_{13}^2 f_{\bar{\nu}_x}^{(\mathrm{a})} + s_{13}^2 f_{\bar{\nu}_y}^{(\mathrm{a})}. \tag{7}$$

For inverted mass hierarchy, the equations are

$$f_{\nu_e}^{(\mathrm{f})} = s_{12}^2 c_{13}^2 f_{\nu_e}^{(\mathrm{a})} + c_{12}^2 c_{13}^2 f_{\nu_x}^{(\mathrm{a})} + s_{13}^2 f_{\nu_y}^{(\mathrm{a})}, \tag{8}$$

$$f_{\bar{\nu}_e}^{(\mathrm{f})} = s_{13}^2 f_{\bar{\nu}_e}^{(\mathrm{a})} + s_{12}^2 c_{13}^2 f_{\bar{\nu}_x}^{(\mathrm{a})} + c_{12}^2 c_{13}^2 f_{\bar{\nu}_y}^{(\mathrm{a})}. \tag{9}$$

In the above equations, c_{ij} and s_{ij} stand for $\cos\theta_{ij}$ and $\sin\theta_{ij}$, respectively. We denote our spectrum after CNO as $f_{\nu}^{(\mathrm{a})}$.[1]

In the case of inverted mass hierarchy, the antineutrino experiences MSW resonances after CNO. At high resonance, $\bar{\nu}_e$ and $\bar{\nu}_y$ are completely swapped. At low resonance, $\bar{\nu}_e$ and $\bar{\nu}_x$ are mixed, and 70% of the $\bar{\nu}_e$ survives. In short, we obtain an approximate equation from Eq. (9):

$$f_{\bar{\nu}_e}^{(\mathrm{f})} \sim 0.7(1-\epsilon) f_{\bar{\nu}_e}^{(\mathrm{o})} + (0.3 + 0.7\epsilon) f_{\bar{\nu}_X}^{(\mathrm{o})}, \tag{10}$$

where $f_{\nu}^{(\mathrm{o})}$ represents the "original flux" and ϵ is the survival probability of $\bar{\nu}_e$ just after CNO, i.e., $f_{\bar{\nu}_e}^{(\mathrm{a})} = \epsilon f_{\bar{\nu}_e}^{(\mathrm{o})} + (1-\epsilon) f_{\bar{\nu}_X}^{(\mathrm{o})}$. Here, conversion between e and y sectors are assumed. Namely, we substituted the following equations into Eq. (9), $f_{\bar{\nu}_y}^{(\mathrm{a})} = (1-\epsilon) f_{\bar{\nu}_e}^{(\mathrm{o})} + \epsilon f_{\bar{\nu}_X}^{(\mathrm{o})}$ and $f_{\bar{\nu}_x}^{(\mathrm{a})} = f_{\bar{\nu}_X}^{(\mathrm{o})}$. This assumption is most valid for the time between 100 ms and 300 ms postbounce. Though $e-x$ and $e-y$ conversions can be seen during this phase (e.g., Fig. 4), the $e-x$ effect is not so prominent in intermediate and high energies relevant for detection.

Roughly speaking, the survival probability of $\bar{\nu}_e$ after the occurrence of CNO is 0.3 for $E > 15$ MeV (see Fig. 3). Substituting $\epsilon = 0.3$ into the equations above, we obtain $f_{\bar{\nu}_e}^{(\mathrm{a})} = 0.3 f_{\bar{\nu}_e}^{(\mathrm{o})} + 0.7 f_{\bar{\nu}_X}^{(\mathrm{o})}$. This can be confirmed in the top panel of Fig. 5. Above ~15 MeV, the red line, $f_{\bar{\nu}_e}^{(\mathrm{a})}$, is closer to the blue line, $f_{\bar{\nu}_X}^{(\mathrm{o})}$. From Eq. (10), we obtain $f_{\bar{\nu}_e}^{(\mathrm{f})} = 0.49 f_{\bar{\nu}_e}^{(\mathrm{o})} + 0.51 f_{\bar{\nu}_X}^{(\mathrm{o})}$ for $\epsilon = 0.3$. This can be confirmed in the bottom panel of Fig. 5, where the red line, $f_{\bar{\nu}_e}^{(\mathrm{f})}$, sits almost at midpoint between the blue line, $f_{\bar{\nu}_X}^{(\mathrm{o})}$, and the green line, $f_{\bar{\nu}_e}^{(\mathrm{o})}$, for this energy range.

1. Detection property of $\bar{\nu}_e$

The neutrinos that reach the Earth can be detected by neutrino observation facilities. The main interaction for $\bar{\nu}_e$ is the inverse-beta decay. The event rate of the inverse-beta decay, $\frac{\mathrm{d}N}{\mathrm{d}t}[1/\mathrm{s}]$, can be evaluated by the following equation[2]:

$$\frac{\mathrm{d}N}{\mathrm{d}t} = N_{\mathrm{tar}} \int_{E_{\mathrm{th}}} F\sigma \mathrm{d}E, \tag{11}$$

where N_{tar} is the number of the target in the detector, E_{th} is the threshold energy of the detector, $F[/\mathrm{MeV}/\mathrm{cm}^2/\mathrm{s}]$ is the number flux of the neutrino at the Earth, and $\sigma[\mathrm{cm}^2]$ is the cross section of the target. The variables in the integral depend on the energy of the neutrino, $E[\mathrm{MeV}]$. It should be noted that F is proportional to the inverse square of the source distance. The fluxes shown in Fig. 5 assume a source distance of 10 kpc, corresponding approximately to the distance to the Galactic center.

For the case of the HK detector, we adopt

$$N_{\mathrm{tar}} = N_{\mathrm{A}} \left(\frac{2M_{\mathrm{H}}}{M_{\mathrm{H_2O}}} \right) \rho_{\mathrm{H_2O}} V, \tag{12}$$

where V is the volume of the detector, set to 220 kton, N_{A} is Avogadro's constant, and $\rho_{\mathrm{H_2O}}$ is the density of water. In the equation, $(\frac{2M_{\mathrm{H}}}{M_{\mathrm{H_2O}}})$ is the mass fraction of hydrogen in $\mathrm{H_2O}$ and it equals $\frac{2}{18}$. We use the cross section of $\sigma = 9.77 \times 10^{-44} (\frac{E}{1[\mathrm{MeV}]})^2$ $[\mathrm{cm}^2]$. Including corrections of order $1/M_p$ to the cross section and kinematics [89] typically yields 10%–20% reduction in event rates depending on detection threshold. The threshold energy is set to $E_{\mathrm{th}} = 8.3$ MeV [90].

Thousand of neutrinos will be detected in every 50 ms bin if a supernova occurs near the Galactic center. The event number in 50 ms bins, N, is shown in the top panel of Fig. 9 by solid lines (the left axis). The definition of the number is $N = \frac{\mathrm{d}N}{\mathrm{d}t} \times \Delta t$ and $\Delta t = 0.05[\mathrm{s}]$. The error bar of the line, $\pm\delta N$, is evaluated by the Poisson error, i.e., $\delta N/N = 1/\sqrt{N}$. The red or blue color represents the event number with or without CNO. Naively, one may expect that the with or without CNO scenarios can be distinguished

[1] In Ref. [50], $f_{\nu}^{(a)}$ is denoted as $f_{\nu}^{(i)}$, where the superscript (i) means the "initial flux." We change the superscript to (a) in order to avoid confusion with the "original flux" before CNO. In our study, neutrinos that have not reached the point of high resonance are labeled as the initial flux that the authors define. See also Eq. (19) for their definition of the variable [50].

[2] Here we ignore the dependence of the kinetic energy of the scattered particle on the cross section. In general, we have to take this into account. For example, in the case of the scattering of a neutrino and an electron, the kinetic energy of the electron should be considered in the equation. In the case of inverse-beta decay, the kinetic energy is identically determined, and we do not have to include it explicitly in the equation.

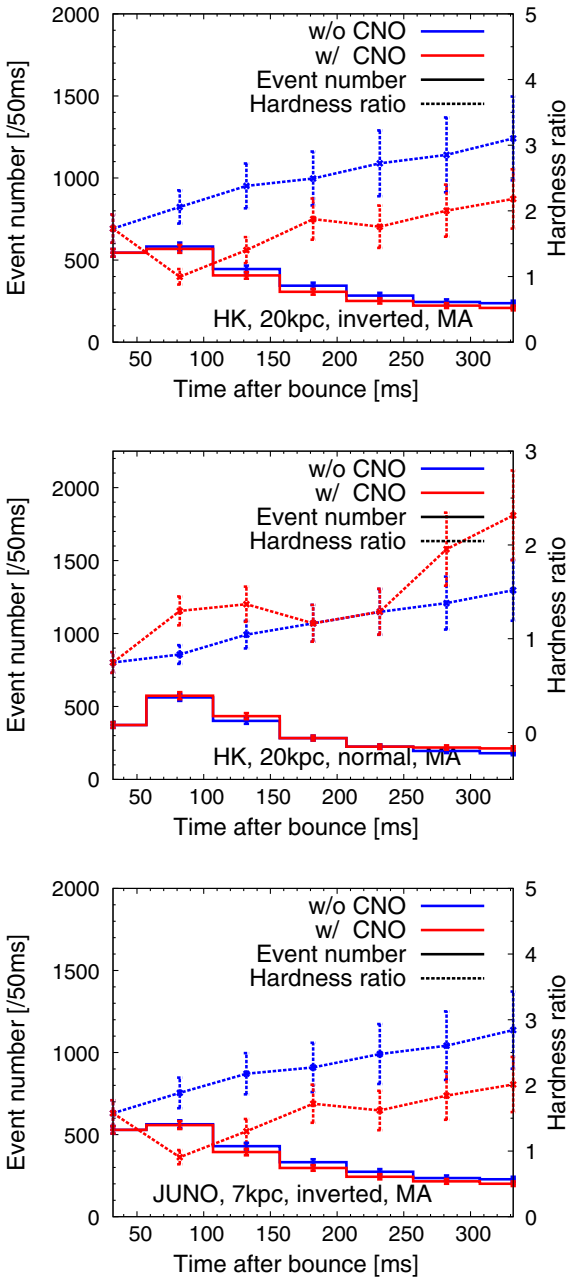

FIG. 9. Evolution of event number in 50 ms bins (solid lines, left axis) and the hardness ratio (dotted lines, right axis). Top: That of HK in the inverted mass hierarchy. A volume of 220 kton is adopted. Middle: That of HK in the normal mass hierarchy. Bottom: That of JUNO in the inverted mass hierarchy. See the text for adopted detector parameters.

since their difference is larger than the Poisson error. However, this neglects other sources of errors coming from our limited knowledge of the progenitor. For example, it is hard to know the detailed structure of the stellar core in reality, which strongly affects the neutrino luminosity [91,92]. If an explosion happens in our Galaxy, the evaluation of its distance is oftentimes difficult. The distance to the supernova can easily change the neutrino luminosity [93]. These uncertainties can be larger than the difference between the with or without CNO scenarios.

While it may be difficult to distinguish the with or without CNO scenarios based solely on the event number, there are ways to circumvent much of the additional systematic uncertainties. To see the effect of CNO, we define the hardness ratio $R_{\mathrm{H/L}}$ following Ref. [94]:

$$R_{\mathrm{H/L}} = \frac{N_{E_c<E}}{N_{E<E_c}}, \tag{13}$$

where $N_{E_c<E}$ and $N_{E<E_c}$ are event numbers whose neutrino energy is above E_c and below E_c, respectively. The error of the ratio is given by the following equation:

$$\begin{aligned}\delta R_{\mathrm{H/L}}/R_{\mathrm{H/L}} &= \frac{\delta N_{E_c<E}}{N_{E_c<E}} + \frac{\delta N_{E<E_c}}{N_{E<E_c}} \\ &= \frac{1}{\sqrt{N_{E_c<E}}} + \frac{1}{\sqrt{N_{E<E_c}}}.\end{aligned} \tag{14}$$

This ratio is sensitive to the neutrino average energy and not sensitive to the integrated flux. This means the error from the stellar structure and distance from the source does not strongly affect the ratio.

The evolution of the hardness ratio with $E_c = 20$ MeV is shown in the top panel of Fig. 9 by dotted lines (the right axis). The blue line corresponds to the ratio without CNO. Due to high resonance MSW, the spectrum of $\bar{\nu}_e$ at the Earth is exactly that of the original ν_X. The red line is depicted with the effect of CNO. CNO changes the spectrum, and some fraction of the original spectrum of $\bar{\nu}_e$ remains in the spectrum at the Earth. Compared to the case without CNO, the spectrum with CNO becomes softer since the average energy of the original $\bar{\nu}_e$ is lower than that of the original ν_X.

When CNO happens, the hardness ratio suddenly becomes smaller. This feature is easy to distinguish from that of the case without CNO since the ratio naturally tends to increase as time goes by. The latter trend is seen in the blue dotted line in the top panel of Fig. 9. During this phase, the neutron star is shrinking. Then, the neutrino spectrum naturally evolves to become hard as the neutrinosphere becomes smaller and the effective temperature becomes higher. Since the effect of CNO is the opposite of this generic trend, it can be easily identified. The error bar of the hardness ratio at the 20 kpc source is less than the difference between the models with and without CNO. We can distinguish the two models even if we take the 1σ Poisson error into account.

In the case of normal mass hierarchy, the hardness ratio of $\bar{\nu}_e$ becomes higher due to the effect of CNO. We calculate the flux at the Earth using Eq. (7). An approximate formula of Eq. (7) is

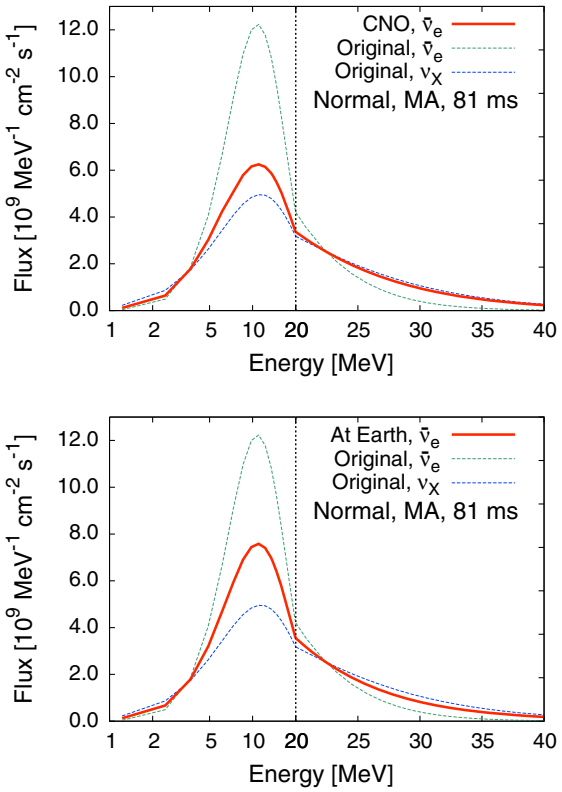

FIG. 10. Same as Fig. 5 but for the normal mass hierarchy. The time snapshot of 81 ms is used.

$$f_{\bar{\nu}_e}^{(\mathrm{f})} \sim (0.3 + 0.4\epsilon) f_{\bar{\nu}_e}^{(\mathrm{o})} + (0.7 - 0.4\epsilon) f_{\bar{\nu}_X}^{(\mathrm{o})}, \qquad (15)$$

where ϵ is the survival probability of $\bar{\nu}_e$ just after CNO (conversion between $e - x$ is assumed). The event rate and the hardness ratio with $E_c = 20$ MeV are given in the middle panel of Fig. 9. The blue line corresponds to the model without CNO, i.e., $\epsilon = 1$. In the normal mass hierarchy, MSW high resonance does not affect the spectrum of $\bar{\nu}_e$, and 70% of $\bar{\nu}_e$ survives at MSW low resonance [see Eq. (15)]. As a result, the spectrum at the Earth is similar to that of the original $\bar{\nu}_e$, and the hardness ratio is low. The red lines show the results with CNO. In this case, CNO decreases the survival probability of $\bar{\nu}_e$. The spectrum of $\bar{\nu}_e$ at the Earth contains a large fraction from the original ν_X. As a result, the hardness ratio becomes higher.

The value of ϵ can be seen in the bottom panel of Fig. 3. The spectra at 81 ms postbounce is shown in Fig. 10. At this time, the survival probability ϵ is 0.2, and a large fraction of the electron antineutrinos are converted to x antineutrinos. The top panel of Fig. 10 shows the spectra after CNO (1500 km). The spectra of electron antineutrinos are closer to that of the original $\bar{\nu}_X$. After CNO, the neutrinos experience MSW low resonance, and the x antineutrinos and electron antineutrinos are mixed. In this case, the x antineutrino contains a large fraction of original $\bar{\nu}_e$, and the electron antineutrino spectrum after MSW low resonance becomes softer. This is shown in the bottom panel of Fig. 10. The electron antineutrino spectrum (red curve) is softer than that after CNO (red curve in the top panel of Fig. 10).

At the onset of CNO, we therefore see a rapid rise of the hardness ratio. Unfortunately, this deviates to the level of degeneracy with the natural rise of the hardness due to the evolution of the protoneutrino star. One would have to compare the rise times of the hardness ratio to draw a robust conclusion. While the error bar of the hardness ratio at a source distance of 20 kpc is smaller than the difference of the models with and without CNO, we have to consider the degeneracy. We conclude that the source distance should be less than ~10 kpc to test the presence of CNO. The statistical error will improve linearly with distance, increasing the potential to distinguish between models. A statistical statement will require us to marginalize over the degeneracy stated above and also work with multiple time bins, which are beyond the scope of this work, but, e.g., a 3σ statement should require distances of less than 3.3 kpc.

The value of the hardness ratio depends on the detector. The event rate and the hardness ratio of JUNO are given in the bottom panel of Fig. 9. Since the energy threshold of JUNO is lower than HK, JUNO can capture low energy neutrinos. Reflecting that feature, the value of the hardness ratio becomes low compared to that of HK. However, the overall features are not so different. Due to the smaller volume of JUNO, the statistical errors are comparable to the difference between the predictions with and without CNO, showing that the source distance should be less than some 5 kpc to distinguish the effect of CNO. We use Eq. (11) to evaluate the event number. We assume that JUNO is a 20 kton detector [95]. First, we evaluate the event rate in KamLAND and later multiply a factor coming from the volume difference of $(20/0.7)$ to obtain the rate in JUNO. The number of target protons in KamLAND N_{tar} is 5.98×10^{31} for each 0.7 kton fiducial volume [96]. It should be noted that KamLAND uses dodecane, and the density and mass ratio for H_2O cannot be applied. The cross section is the same as that of HK. The energy threshold is 1.8 MeV.

2. Detection property of ν_e

CNO is also expected in the electron neutrinos, where the oscillation property is as interesting as that of electron antineutrinos. Although it is difficult to detect larger numbers of clean ν_e's with detectors currently in operation, the future large-volume liquid argon detector, DUNE, is expected to change this. To prepare for this era, we next predict the oscillation property in ν_e.

The top panel of Fig. 11 shows the spectrum in the case of the inverted mass hierarchy. After CNO, the neutrinos experience the MSW low resonance, and 30% of the ν_e survives. From Eq. (8),

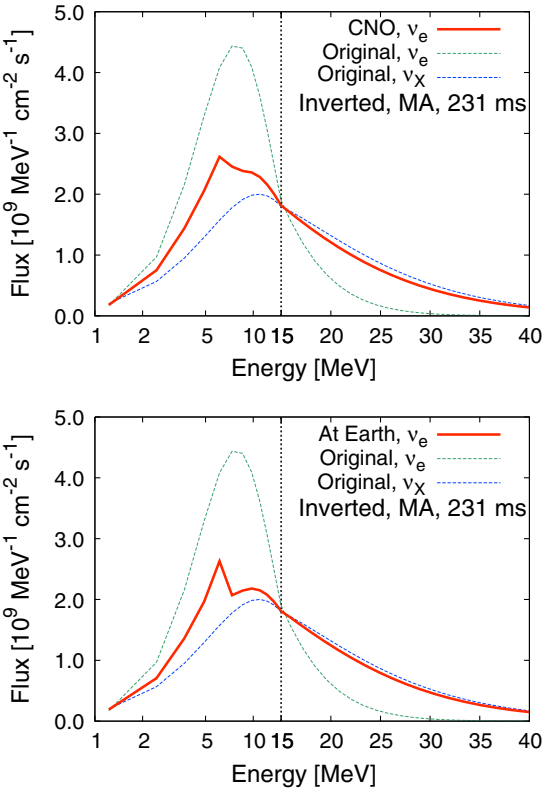

FIG. 11. Same as Fig. 5, but for electron neutrinos. Note that in both panels, the horizontal axis is logarithmic for $E < 15$ MeV and linear for $E > 15$ MeV in the both panels (indicated by the vertical dashed line).

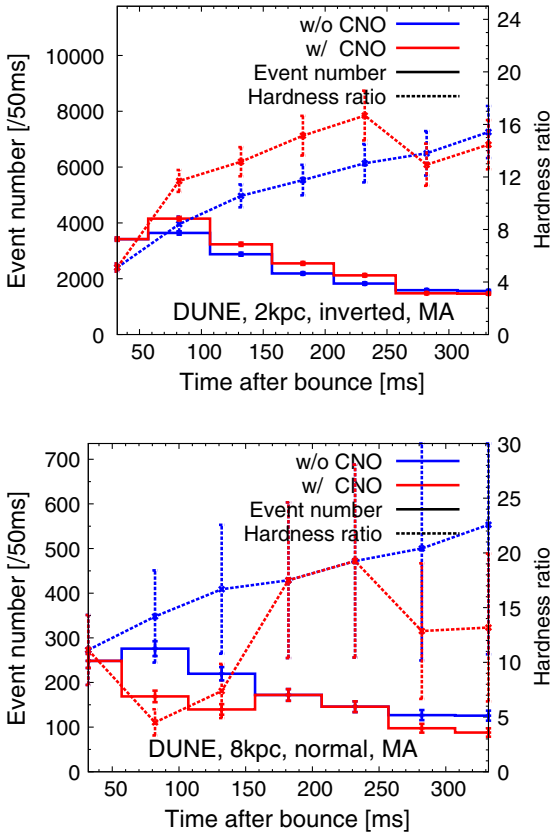

FIG. 12. Event number and hardness ratio in 50 ms bins, both for ν_e detected by DUNE. Note that a lower E_c is adopted than that in Fig. 9. Top panel: The case of inverted mass hierarchy and a source distance of 2 kpc. Bottom panel: The case of normal mass hierarchy and a source distance of 8 kpc.

$$f_{\nu_e}^{(\mathrm{f})} \sim 0.3\epsilon f_{\nu_e}^{(\mathrm{o})} + (1.0 - 0.3\epsilon) f_{\nu_X}^{(\mathrm{o})}, \tag{16}$$

where ϵ is the survival probability just after CNO ($e - y$ conversion is assumed). MSW low resonance significantly makes the fraction of the original ν_e at the Earth lower: If CNO does not happen, the fraction is maximum at 30%, and CNO makes the fraction lower. The bottom panel of Fig. 11 shows the spectrum at the Earth. The spectrum (red curve) almost looks like that of the original ν_X (blue curve).

For normal mass hierarchy, we obtain an approximate formula from Eq. (6) by a similar analysis as above:

$$f_{\nu_e}^{(\mathrm{f})} \sim (0.7 - 0.7\epsilon) f_{\nu_e}^{(\mathrm{o})} + (0.3 + 0.7\epsilon) f_{\nu_X}^{(\mathrm{o})}, \tag{17}$$

where ϵ is the survival probability just after CNO ($e - x$ conversion is assumed).

The ν_e emitted in the supernova can be detected in large numbers. Of the existing and planned neutrino detectors, DUNE is the primary detector with an expected high-statistics clean ν_e signal [97]. We use the cross section of the primary charge-current interaction on liquid argon, $\nu_e + {}^{40}\mathrm{Ar} \to e^- + {}^{40}\mathrm{K}^*$, based on the random phase approximation scheme of Ref. [98]. Using Eq. (11), we compute the event rates due to this reaction. We evaluate the number of the target nuclei, taking DUNE's total fiducial volume to be 40 kton. We adopt a detection threshold of 5 MeV ν_e energy and, for simplicity, assume a detection efficiency of 100%. The true threshold and efficiency remain to be determined. In reality, the low energy of the supernova neutrino means that the interaction products may only leave stublike tracks and blips in the liquid argon time-projection chamber; also, the signal may be vulnerable to radioactive and cosmogenic backgrounds [99]. More work is underway to understand the efficiency as a function of detector configuration. We estimate the number of events in 50 ms bins and the hardness ratio with $E_c = 15$ MeV, and show their time evolutions in Fig. 12.

In the case of inverted mass hierarchy, the spectrum of ν_e becomes hard after CNO. In the top panel of Fig. 12, the blue (red) line is the event number and the hardness ratio without (with) CNO. Equation (16) shows that the CNO decreases the fraction of the original ν_e in the spectrum at the Earth and increases the fraction of the original ν_X. As a result, the spectrum becomes hard after CNO occurs. That feature appears before 281 ms. In the later explosion phase, such as at 331 and 381 ms, however, $x - y$ mixing after $e - y$ conversion as shown in the bottom panel of Fig. 4

occurs actively in the neutrino sector. Such prominent three-flavor mixing makes the hardness ratio of ν_e small in the inverted mass hierarchy. This behavior can be explained by considering the survival probability η in the $x-y$ conversions. The final ν_e flux on the Earth is described by

$$f_{\nu_e}^{(\mathrm{f})} \sim [0.3\epsilon + 0.7(1-\eta)(1-\epsilon)]f_{\nu_e}^{(\mathrm{o})} + [1.0 - 0.3\epsilon - 0.7(1-\eta)(1-\epsilon)]f_{\nu_X}^{(\mathrm{o})}, \quad (18)$$

which reproduces Eq. (16) under the two-flavor limit in the $e-y$ sector ($\eta \to 1$). As shown in Eq. (18), three-flavor mixing ($0 \le \eta < 1$) increases the fraction of original ν_e, which prevents a hard ν_e spectrum at the Earth. To make the error bar of the hardness ratio smaller than the model difference, the source distance should be less than ∼2 kpc.

On the other hand, CNO makes the spectrum soft in the case of normal mass hierarchy regardless of three-flavor mixing. The bottom panel of Fig. 12 shows the time evolution of the event rate and the hardness ratio for the normal mass hierarchy. The blue line is without CNO, i.e., $\epsilon = 1$ in Eq. (17). Here, the survival probability of ν_e at the Earth is 0 with the MSW high resonance. CNO cancels the effect of the MSW high resonance. Then, the survival probability becomes finite and at most 70% [see Eq. (17) and substitute $\epsilon = 0$]. Although the MSW low resonance also decreases the survival probability, a fraction of the original ν_e still remains at the Earth. This makes the spectrum soft. Since the amplitude of this softening is large compared to the error bar of the hardness ratio, the statistical errors remain smaller than the model difference out to source distances of ∼8 kpc.

Compared to the case of HK, we need a closer source distance to distinguish the effect of CNO in DUNE. The larger statistical error originates from the smaller $N_{E<E_c}$. Since we do not optimize the value of E_c here, changing the value of E_c could decrease the error in future studies.

3. Synergistic observation

We summarize the effect of CNO in Table I. In the case of the inverted mass hierarchy, the $\bar{\nu}_e$ spectrum without CNO is hard since the original ν_X spectrum is observed at the Earth (see the second column of the third row). The spectrum becomes soft if CNO takes place (see the third column of the third row). On the other hand, the spectrum of ν_e is soft before the occurrence of CNO [see Eq. (16)].

TABLE I. Summary of the effect of CNO. See text for the meaning of $*$.

Hierarchy	Inverted	Inverted	Normal	Normal
CNO	Off	On	Off	On
$\bar{\nu}_e$ spectrum	Hard	Soft	Soft	Hard
ν_e spectrum	Soft	Hard*	Hard	Soft

Here, CNO makes the spectrum hard before the three-flavor mixing in CNO is switched on. After the nonlinear three-flavor mixing, the fraction of the original ν_e increases, and the spectrum becomes soft (see the third column of the fourth row). This complicated behavior is noted with an asterisk in the table.

The role of CNO in the normal mass hierarchy has the opposite effect as in the inverted mass hierarchy. Namely, the soft spectrum of $\bar{\nu}_e$ becomes harder with the onset of CNO. The CNO makes the hard spectrum of ν_e softer. These are summarized in the last two columns of Table I.

Interestingly, the effect of CNO is such that when the spectrum of $\bar{\nu}_e$ is harder, that of ν_e is softer. This means synergistic observations of $\bar{\nu}_e$ and ν_e would be valuable to look for the occurrence of CNO. In this respect, the results from HK and DUNE will complement each other very strongly. The horizon for joint observation appears to be slightly smaller than 10 kpc. For example, DUNE may capture the onset of CNO in the inverted mass hierarchy for sources closer than ∼2 kpc (see top panel of Fig. 12).

IV. SUMMARY AND DISCUSSION

We performed a neutrino radiation hydrodynamic simulation of a 8.8 $M_\odot$ progenitor and used the profile of the simulation to investigate the impact of CNO on the detected neutrinos on the Earth. We considered HK, JUNO, and DUNE, and evaluated detectability defining a hardness ratio of the observed neutrino spectra. Our findings are summarized as follows.

(i) CNO happens 100 ms after bounce; it is suppressed by matter-induced decoherence before this time. The dilute envelope structure of the progenitor is the main reason for such an early emergence of CNO. The precise time can be affected by the spectral shape.

(ii) In the case of inverted mass hierarchy, the spectrum of $\bar{\nu}_e$ becomes softer after CNO sets in. The hardness ratio that we defined in Eq. (13) is helpful to identify the onset of the CNO effect. HK can distinguish this effect when the supernova happens within a distance of ∼10 kpc.

(iii) In the case of normal mass hierarchy, the spectrum of ν_e becomes softer after CNO happens. DUNE can distinguish this effect when the supernova happens within a distance of ∼10 kpc.

(iv) If the spectrum of $\bar{\nu}_e$ becomes softer due to CNO, the spectrum of ν_e becomes harder (and vice versa). This provides a synergistic opportunity to combine the $\bar{\nu}_e$ and ν_e from HK and DUNE as a valuable method to test the occurrence of CNO.

There are several limitations in this study. First, we finished our hydrodynamic simulations at 331 ms after bounce since the density of the envelope becomes too low and protrudes the region of our tabulated EoS. Thus, we cannot investigate how long this CNO continues. Second,

for the neutrino oscillation part, we have not included the effect of the neutrino-nucleon interactions [100], the feedback of the oscillation to the hydrodynamics [101], the effect of the halo [102,103], multi-azimuthal-angle instability [104], fast flavor conversion [105–108], and nonstandard neutrino self-interactions [109,110], all of which can affect the resulting patterns. More studies will be needed to elucidate their effects and to draw robust conclusions about their detectability and differentiation.

ACKNOWLEDGMENTS

This study was supported in part by the Grants-in-Aid for the Scientific Research of Japan Society for the Promotion of Science (JSPS, No. JP17H01130, No. JP17K14306, No. JP17K17655, No. JP19J13632, and No. JP18H01212), the Ministry of Education, Science and Culture of Japan (MEXT, No. JP15H01039, No. JP17H06357, No. JP17H06364, No. JP17H05206, No. JP26104001, No. JP26104007, and No. JP19H05803), and JICFuS as a priority issue to be tackled by using the Post 'K' Computer. This work is also supported by the NINS program for cross-disciplinary study (Grants No. 01321802 and No. 01311904) on Turbulence, Transport, and Heating Dynamics in Laboratory and Solar/Astrophysical Plasmas: "SoLaBo-X." The work of S. H. is supported by the US Department of Energy Office of Science under Award No. DE-SC0020262, NSF Grant No. AST-1908960, and NSF Grant No. PHY-1914409.

APPENDIX A: DEPENDENCE OF POSITION OF NEUTRINOSPHERE

In our simulations, we employ the single-bulb model and use a fixed neutrinosphere radius of $R = 30$ km irrespective of the postbounce time [42]. We should keep in mind that, originally, the neutrinosphere radius depends on the explosion time, as well as the neutrino energy and neutrino species. Further study is required to consider all of these effects on the CNO. Some previous works [111–113] employ a multibulb model which incorporates the flavor dependence in the neutrinosphere. Here, we show the impacts of the neutrinosphere radius, using the simple bulb model but by changing the radius of the neutrinosphere from 30 km to 50 km. Since the neutrinosphere radius continues to shrink with postbounce time, our simple demonstration is helpful to understand the uncertainty caused by the time evolution of the neutrinosphere.

Figure 13 shows the evolution of survival probabilities of $\bar{\nu}_e$ in the inverted mass hierarchy at 181 ms. In this explosion epoch, CNO can be regarded as two-flavor oscillations in the $e-y$ sector because of the decoupling of the x-type neutrinos. The onset of CNO is 455(570) km in the case of $R = 30(50)$ km. Such delayed nonlinear effects in the large neutrinosphere radius are well explained by the relation between the neutrinosphere radius

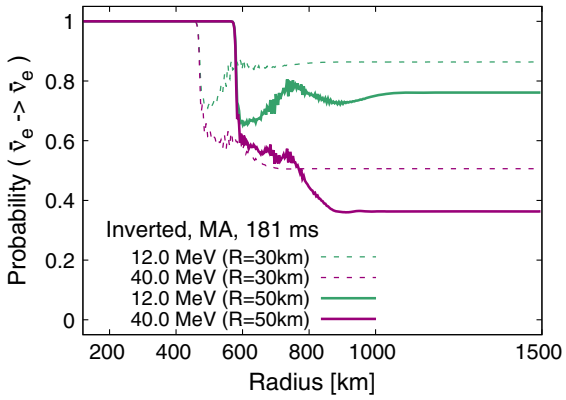

FIG. 13. The comparison of conversion probabilities of $\bar{\nu}_e$ in the inverted mass hierarchy at 181 ms postbounce. The solid (dashed) lines represent radial profiles of conversion probabilities in the bulb model assuming $R = 30(50)$ km.

and instability radius: $r_{\rm inst} \propto R^{1/2}$ [73]. In multiangle simulations, significant nonlinear flavor transitions occur when the dispersions of nonlinear self-interactions are comparable to that of the vacuum Hamiltonian [73].

Final values of survival probabilities after CNO ($r > 1000$ km) are also sensitive to the neutrinosphere radius. Flavor mixings in the larger neutrinosphere ($R = 50$ km) are more prominent than in the smaller radius model ($R = 30$ km). The strength of the matter potential is smaller in the outer region because of decreasing baryon density. The angular dispersion in the matter potential [73,82] does not suppress the coherence of nonlinear flavor transitions if the onset of flavor transitions is delayed. Therefore, CNO occurs more actively in the large neutrinosphere model. A spectral swap after CNO can be seen in Fig. 14. The spectra of electron antineutrinos in both models are similar in the low energy region ($E < E_c = 20$ MeV). However, at high energies ($E > E_c$), the spectrum of $\bar{\nu}_e$ is slightly closer to the original spectrum of $\bar{\nu}_X$ in the

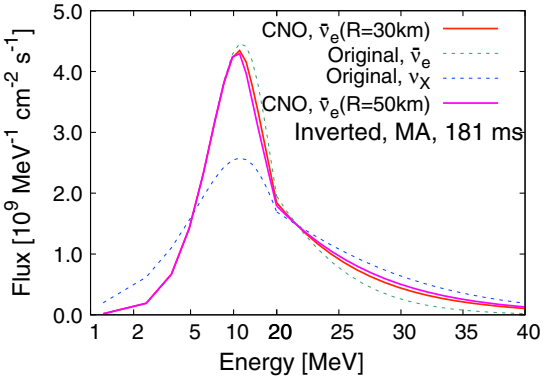

FIG. 14. Comparison of $\bar{\nu}_e$ spectra after CNO. The red (magenta) line represents $\bar{\nu}_e$ spectra after CNO in the $R = 30(50)$ km model. As in Fig. 5, the flux is scaled to that for the 10 kpc source.

$R = 50$ km model compared with the $R = 30$ km model. This enhanced spectral swap reflects active nonlinear flavor transitions without suffering from strong multiangle matter suppression as shown in Fig. 13. Such increased energetic $\bar{\nu}_e$ in the $R = 50$ km model makes the hardness ratio of $\bar{\nu}_e$ softer, which would be helpful to distinguish the effect of CNO.

So far, we have shown the result of CNO at 181 ms by imposing $R = 50$ km, but properties of delayed CNO as confirmed in Figs. 13 and 14 are also common in other explosion phases. The neutrinosphere radius becomes smaller as the explosion proceeds. Therefore, it seems that the hardness ratio of $\bar{\nu}_e$ as shown in Fig. 9 tends to be softer (harder) in earlier (later) explosion phases, respectively, if we consider the time evolution of the neutrinosphere radius. In the normal mass hierarchy, the hardness ratio of ν_e would show such a trend.

APPENDIX B: FERMI-DIRAC SPECTRA

In this Appendix, we show the neutrino oscillation properties using nondegenerate Fermi-Dirac (FD) spectra as the initial spectra. While we adopted a Gamma distribution [76] as the initial spectra in the main body of this paper, another popular choice is the FD distribution [69]. The initial neutrino spectra at the neutrinosphere are set by $\alpha_i = 2$ in Eq. (1), and only the mean average energy of neutrinos is used to define the spectra (see middle panel of Fig. 2 for the mean average energies).

The biggest difference from the Gamma distribution is the time of onset of CNO. Figure 15 shows the survival probabilities as functions of time and neutrino energy. The top panel is for the inverted mass hierarchy. In this case, CNO appears about 200 ms after bounce, which is 100 ms longer than the Gamma spectra (compare top panels of Figs. 3 and 15).

The delayed start of CNO features with the FD spectrum also appears in the normal mass hierarchy. The bottom panel of Fig. 15 shows the survival probabilities as functions of time and neutrino energy in the case of the normal mass hierarchy. CNO features first appear at about 300 ms, while the corresponding features in the case of the Gamma distribution appear at 100 ms (see the bottom panel of Fig. 3).

Furthermore, we evaluate the predicted event rate at HK and the hardness ratio in the case of FD spectra. The spectrum at the Earth can be obtained by Eq. (9). The predicted event number and the hardness ratio are calculated by Eqs. (11) and (13), respectively. Figure 16 shows the time evolution of the event number and the hardness ratio in the 50 ms bin.

CNO makes the spectrum of $\bar{\nu}_e$ at the Earth softer in the inverted mass hierarchy. In the top panel of Fig. 16, the hardness ratio drops after the onset of CNO. This is

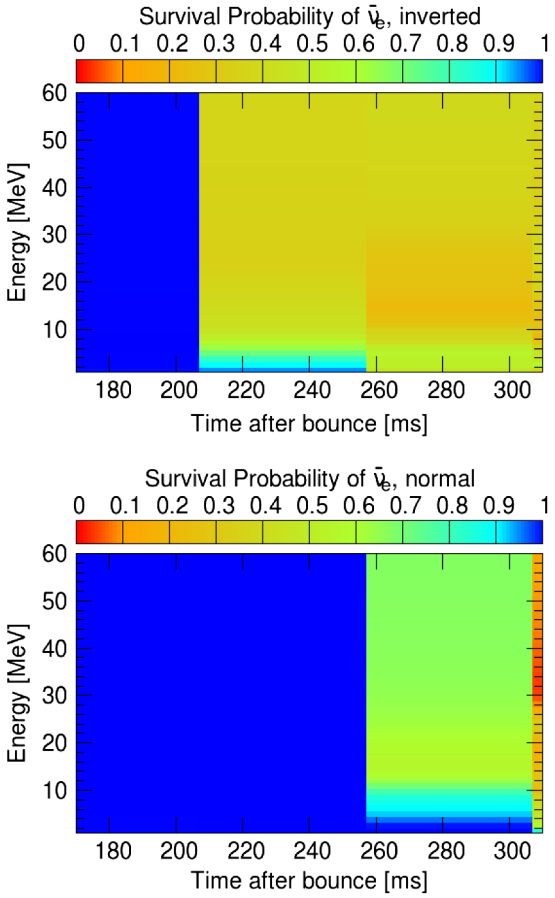

FIG. 15. Same as Fig. 3 but with nondegenerate Fermi-Dirac distributions for the initial neutrino spectra.

qualitatively the same as for the Gamma distribution's initial spectra (see top panel of Fig. 9). Quantitatively, the impact of CNO with the FD spectra is smaller since the initial spectrum of $\bar{\nu}_e$ is more similar to that of $\bar{\nu}_X$. The hardness ratio drops only ∼0.5 in the FD case. By comparison, in the case of the Gamma distribution, the impact is more significant, and the drop is ∼1.0 (see top panel of Fig. 9).

On the other hand, in the case of the normal mass hierarchy, CNO makes the spectrum of $\bar{\nu}_e$ at the Earth harder. The bottom panel of Fig. 16 shows the evolution of the hardness ratio. In this case, the rise of the hardness ratio is ∼1.0 at 300 ms, and the impact is similar to that of the Gamma distribution spectra (see middle panel of Fig. 9).

As in the main body of this article, we can also calculate CNO of ν_e using the FD initial spectra and evaluate the event rate in DUNE. The results are shown in Fig. 17. In the inverted mass hierarchy, the spectrum at the Earth becomes harder when CNO starts. That is essentially the same as the results with the Gamma distribution spectrum (see the top panel of Fig. 12). Similar to $\bar{\nu}_e$, the impact of CNO is smaller compared to the Gamma distribution spectrum

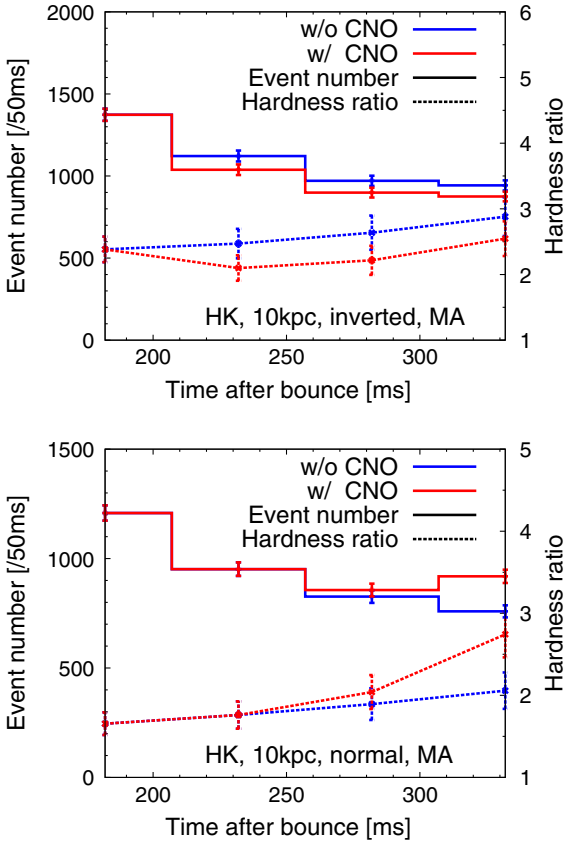

FIG. 16. Same as Fig. 9 but for the FD initial spectra. Different from Fig. 9, the result for JUNO is omitted. Note that the source distance is assumed to be 10 kpc, while 20 kpc is used in Fig. 9.

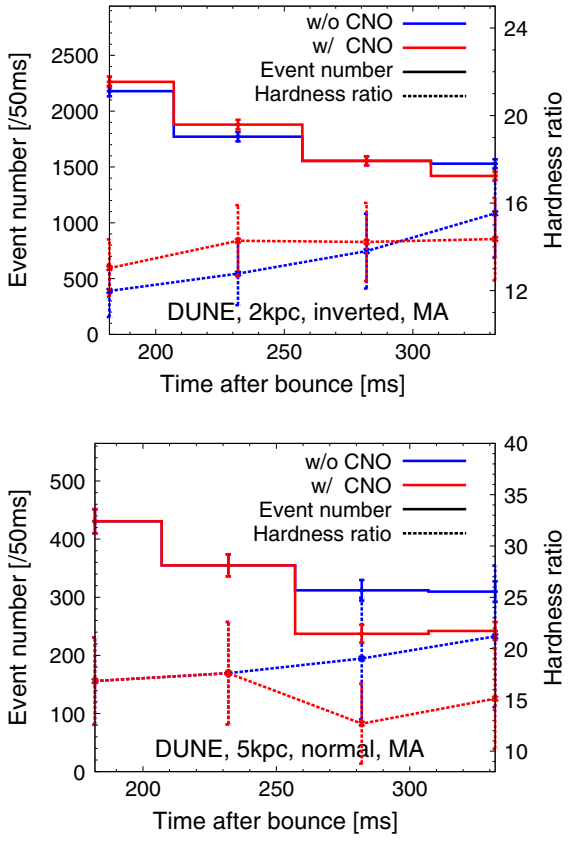

FIG. 17. Same as Fig. 12 but for the FD initial spectra.

since the spectral shapes of ν_e and ν_X are more similar to each other when adopting the FD initial spectra. The rise of the hardness ratio due to CNO is ∼2 at 231 ms with the FD spectra and ∼4 with the Gamma spectra. The results for the normal mass hierarchy are shown in the bottom panel of Fig. 17. Here, CNO decreases the hardness ratio of ν_e. Similar to the inverted mass hierarchy, the impact of CNO with the FD spectra is smaller compared to that with the Gamma spectra.

[1] G. Raffelt, *Proceedings of the International School of Physics "Enrico Fermi"* (IOS Press, 2012), Vol. 182, p. 61–143.
[2] S. Horiuchi and J. P. Kneller, J. Phys. G **45**, 043002 (2018).
[3] H. T. Janka, arXiv:1702.08713.
[4] W. R. Hix, E. J. Lentz, S. W. Bruenn, A. Mezzacappa, O. E. B. Messer, E. Endeve, J. M. Blondin, J. A. Harris, P. Marronetti, and K. N. Yakunin, Acta Phys. Pol. B **47**, 645 (2016).
[5] B. Müller, Pub. Astron. Soc. Aust. **33**, e048 (2016).
[6] A. Mirizzi *et al.*, Riv. Nuovo Cimento **39**, 1 (2015).
[7] T. Foglizzo *et al.*, Pub. Astron. Soc. Aust. **32** (2015).
[8] A. Burrows, Rev. Mod. Phys. **85**, 245 (2013).
[9] K. Kotake, K. Sumiyoshi, S. Yamada, T. Takiwaki, T. Kuroda, Y. Suwa, and H. Nagakura, Prog. Theor. Exp. Phys. **2012** (2012).
[10] M. Ikeda *et al.* (Super-Kamiokande Collaboration), Astrophys. J. **669**, 519 (2007).
[11] R. Abbasi *et al.*, Astron. Astrophys.**535**, A109 (2011).
[12] R. Bruijn, Nucl. Phys. B, Proc. Suppl. **237–238**, 94 (2013).
[13] M. Salathe, M. Ribordy, and L. Demirörs, Astropart. Phys. **35**, 485 (2012).
[14] K. Asakura *et al.*, Astrophys. J. **818**, 91 (2016).
[15] C. Xu, J. Phys. Conf. Ser. **718**, 062070 (2016).
[16] T. Lund, A. Marek, C. Lunardini, H.-T. Janka, and G. Raffelt, Phys. Rev. D **82**, 063007 (2010).

[17] H.-K. Proto-Collaboration *et al.*, arXiv:1805.04163.
[18] Y.-F. Li, Int. J. Mod. Phys. Conf. Ser. **31**, 1460300 (2014).
[19] R. Acciarri *et al.*, arXiv:1601.05471.
[20] S. W. Bruenn, Astrophys. J. Suppl. Ser. **58**, 771 (1985).
[21] M. Liebendörfer, A. Mezzacappa, and F.-K. Thielemann, Phys. Rev. D **63**, 104003 (2001).
[22] M. Rampp and H.-T. Janka, Astron. Astrophys. **396**, 361 (2002).
[23] R. Buras, M. Rampp, H.-T. Janka, and K. Kifonidis, Astron. Astrophys. **447**, 1049 (2006).
[24] M. Shibata, K. Kiuchi, Y.-i. Sekiguchi, and Y. Suwa, Prog. Theor. Phys. **125**, 1255 (2011).
[25] T. Kuroda, T. Takiwaki, and K. Kotake, Astrophys. J. Suppl. Ser. **222**, 20 (2016).
[26] K. Sumiyoshi and S. Yamada, Astrophys. J. Suppl. Ser. **199**, 17 (2012).
[27] T. Takiwaki, K. Kotake, and Y. Suwa, Astrophys. J. **749** (2012).
[28] T. Takiwaki, K. Kotake, and Y. Suwa, Astrophys. J. **786**, 83 (2014).
[29] T. Takiwaki, K. Kotake, and Y. Suwa, Mon. Not. R. Astron. Soc. Lett. **461**, L112 (2016).
[30] F. Hanke, B. Müller, A. Wongwathanarat, A. Marek, and H.-T. Janka, Astrophys. J. **770**, 66 (2013).
[31] I. Tamborra, G. Raffelt, F. Hanke, H.-T. Janka, and B. Müller, Phys. Rev. D **90**, 045032 (2014).
[32] T. Melson, H.-T. Janka, R. Bollig, F. Hanke, A. Marek, and B. Müller, Astrophys. J. Lett. **808**, L42 (2015).
[33] T. Melson, H.-T. Janka, and A. Marek, Astrophys. J. Lett. **801**, L24 (2015).
[34] D. Vartanyan, A. Burrows, D. Radice, M. A. Skinner, and J. Dolence, Mon. Not. R. Astron. Soc. **482**, 351 (2019).
[35] L. Walk, I. Tamborra, H.-T. Janka, and A. Summa, Phys. Rev. D **98**, 123001 (2018).
[36] I. Tamborra, F. Hanke, H.-T. Janka, B. Müller, G. G. Raffelt, and A. Marek, Astrophys. J. **792**, 96 (2014).
[37] T. Takiwaki and K. Kotake, Mon. Not. R. Astron. Soc. Lett. **475**, L91 (2018).
[38] H. Duan and J. P. Kneller, J. Phys. G **36**, 113201 (2009).
[39] L. Wolfenstein, Phys. Rev. D **17**, 2369 (1978).
[40] S. P. Mikheyev and A. Yu. Smirnov, Sov. J. Nucl. Phys. **42**, 913 (1985).
[41] H. Duan, G. M. Fuller, J. Carlson, and Y.-Z. Qian, Phys. Rev. Lett. **97**, 241101 (2006).
[42] H. Duan, G. M. Fuller, and Y.-Z. Qian, Phys. Rev. D **74**, 123004 (2006).
[43] G. Fogli, E. Lisi, A. Marrone, and I. Tamborra, J. Cosmol. Astropart. Phys. 04 (2009) 030.
[44] Daya Bay Collaboration *et al.*, Phys. Rev. Lett. **112**, 061801 (2014).
[45] S. Chakraborty, T. Fischer, A. Mirizzi, N. Saviano, and R. Tomàs, Phys. Rev. Lett. **107**, 151101 (2011).
[46] S. Chakraborty, T. Fischer, A. Mirizzi, N. Saviano, and R. Tomàs, Phys. Rev. D **84**, 025002 (2011).
[47] Y. Suwa, K. Kotake, T. Takiwaki, M. Liebendörfer, and K. Sato, Astrophys. J. **738**, 165 (2011).
[48] N. Saviano, S. Chakraborty, T. Fischer, and A. Mirizzi, Phys. Rev. D **85**, 113002 (2012).
[49] S. Sarikas, G. G. Raffelt, L. Hüdepohl, and H.-T. Janka, Phys. Rev. Lett. **108**, 061101 (2012).
[50] M.-R. Wu, Y.-Z. Qian, G. Martínez-Pinedo, T. Fischer, and L. Huther, Phys. Rev. D **91**, 065016 (2015).
[51] B. Dasgupta, E. O'Connor, and C. D. Ott, Phys. Rev. D **85**, 065008 (2012).
[52] H. Sasaki, T. Kajino, T. Takiwaki, T. Hayakawa, A. B. Balantekin, and Y. Pehlivan, Phys. Rev. D **96**, 043013 (2017).
[53] M. Zaizen, T. Yoshida, K. Sumiyoshi, and H. Umeda, Phys. Rev. D **98**, 103020 (2018).
[54] C. J. Horowitz, O. L. Caballero, Z. Lin, E. O'Connor, and A. Schwenk, Phys. Rev. C **95**, 025801 (2017).
[55] C. J. Horowitz, Phys. Rev. D **65**, 043001 (2002).
[56] K. Kotake, T. Takiwaki, T. Fischer, K. Nakamura, and G. Martínez-Pinedo, Astrophys. J. **853**, 170 (2018).
[57] E. O'Connor *et al.*, J. Phys. G **45**, 104001 (2018).
[58] K. Nakamura, S. Horiuchi, M. Tanaka, K. Hayama, T. Takiwaki, and K. Kotake, Mon. Not. R. Astron. Soc. **461** (2016).
[59] H. Sotani and T. Takiwaki, Phys. Rev. D **94**, 044043 (2016).
[60] K. Nakamura, T. Takiwaki, T. Kuroda, and K. Kotake, Publ. Astron. Soc. Jpn. **67**, 107 (2015).
[61] A. Mignone, J. Comput. Phys. **270**, 784 (2014).
[62] E. F. Toro, M. Spruce, and W. Speares, Shock Waves **4**, 25 (1994).
[63] J. M. Lattimer and F. Douglas Swesty, Nucl. Phys. **A535**, 331 (1991).
[64] M. Liebendörfer, S. C. Whitehouse, and T. Fischer, Astrophys. J. **698**, 1174 (2009).
[65] K. Nomoto, Astrophys. J. **277**, 791 (1984).
[66] K. Nomoto, Astrophys. J. **322**, 206 (1987).
[67] N. Tominaga, S. I. Blinnikov, and K. Nomoto, Astrophys. J. **771**, L12 (2013).
[68] F. S. Kitaura, H.-T. Janka, and W. Hillebrandt, Astron. Astrophys. **450**, 345 (2006).
[69] G. L. Fogli, E. Lisi, A. Marrone, and A. Mirizzi, J. Cosmol. Astropart. Phys. 12 (2007) 010.
[70] B. Dasgupta, A. Dighe, G. G. Raffelt, and A. Yu. Smirnov, Phys. Rev. Lett. **103**, 051105 (2009).
[71] B. Dasgupta, A. Mirizzi, I. Tamborra, and R. Tomas, Phys. Rev. D **81**, 093008 (2010).
[72] A. Mirizzi and R. Tomas, Phys. Rev. D **84**, 033013 (2011).
[73] H. Duan and A. Friedland, Phys. Rev. Lett. **106**, 091101 (2011).
[74] S. Birol, Y. Pehlivan, A. B. Balantekin, and T. Kajino, Phys. Rev. D **98**, 083002 (2018).
[75] A. Esteban-Pretel, S. Pastor, R. Tomas, G. G. Raffelt, and G. Sigl, Phys. Rev. D **76**, 125018 (2007).
[76] I. Tamborra, B. Müller, L. Hüdepohl, H.-T. Janka, and G. Raffelt, Phys. Rev. D **86**, 125031 (2012).
[77] A. Summa, F. Hanke, H.-T. Janka, T. Melson, A. Marek, and B. Müller, Astrophys. J. **825**, 6 (2016).
[78] T. Yoshida, Y. Suwa, H. Umeda, M. Shibata, and K. Takahashi, Mon. Not. R. Astron. Soc. **471**, 4275 (2017).
[79] H.-T. Janka, B. Müller, F. S. Kitaura, and R. Buras, Astron. Astrophys. **485**, 199 (2008).
[80] T. Fischer, S. C. Whitehouse, A. Mezzacappa, F.-K. Thielemann, and M. Liebendörfer, Astron. Astrophys. **517**, A80 (2010).

[81] B. Dasgupta and A. Dighe, Phys. Rev. D **77**, 113002 (2008).
[82] A. Esteban-Pretel, A. Mirizzi, S. Pastor, R. Tomàs, G. G. Raffelt, P. D. Serpico, and G. Sigl, Phys. Rev. D **78**, 085012 (2008).
[83] B. Dasgupta, A. Dighe, A. Mirizzi, and G. G. Raffelt, Phys. Rev. D **77**, 113007 (2008).
[84] H. Duan, G. M. Fuller, J. Carlson, and Y.-Z. Qian, Phys. Rev. Lett. **100**, 021101 (2008).
[85] J. F. Cherry, G. M. Fuller, J. Carlson, H. Duan, and Y.-Z. Qian, Phys. Rev. D **82**, 085025 (2010).
[86] C. Döring, R. S. L. Hansen, and M. Lindner, J. Cosmol. Astropart. Phys. 08 (2019) 003.
[87] S. Hannestad, G. G. Raffelt, G. Sigl, and Y. Y. Y. Wong, Phys. Rev. D **74**, 105010 (2006); **76**, 029901(E) (2007).
[88] M. Tanabashi *et al.* (Particle Data Group), Phys. Rev. D **98**, 030001 (2018), and 2019 update.
[89] P. Vogel and J. F. Beacom, Phys. Rev. D **60**, 053003 (1999).
[90] C. Kato, H. Nagakura, S. Furusawa, K. Takahashi, H. Umeda, T. Yoshida, K. Ishidoshiro, and S. Yamada, Astrophys. J. **848**, 48 (2017).
[91] E. O'Connor and C. D. Ott, Astrophys. J. **762**, 126 (2013).
[92] K. Nakazato *et al.*, Astrophys. J. Suppl. Ser. **205**, 2 (2013).
[93] S. Horiuchi, K. Nakamura, T. Takiwaki, and K. Kotake, J. Phys. G **44**, 114001 (2017).
[94] S. Kawagoe, T. Takiwaki, and K. Kotake, J. Cosmol. Astropart. Phys. 09 (2009) 033.
[95] F. An *et al.*, J. Phys. G **43**, 030401 (2016).
[96] A. Gando *et al.*, Astrophys. J. **829**, L34 (2016).
[97] K. Scholberg, Annu. Rev. Nucl. Part. Sci. **62**, 81 (2012).
[98] E. Kolbe, K. Langanke, G. Martínez-Pinedo, and P. Vogel, J. Phys. G **29**, 2569 (2003).
[99] A. Ankowski *et al.*, Supernova physics at DUNE, in *Supernova Physics at DUNE* Blacksburg, Virginia, USA (2016).
[100] S. Shalgar and I. Tamborra, Astrophys. J. **883**, 80 (2019).
[101] C. J. Stapleford, C. Fröhlich, and J. P. Kneller, arXiv: 1910.04172.
[102] J. F. Cherry, J. Carlson, A. Friedland, G. M. Fuller, and A. Vlasenko, Phys. Rev. D **87**, 085037 (2013).
[103] M. Zaizen *et al.*, arXiv:1908.10594.
[104] R. F. Sawyer, Phys. Rev. D **79**, 105003 (2009).
[105] S. Abbar, H. Duan, K. Sumiyoshi, T. Takiwaki, and M. C. Volpe, Phys. Rev. D **100**, 043004 (2019).
[106] S. Abbar, H. Duan, K. Sumiyoshi, T. Takiwaki, and M. C. Volpe, arXiv:1911.01983.
[107] M. D. Azari, S. Yamada, T. Morinaga, W. Iwakami, H. Okawa, H. Nagakura, and K. Sumiyoshi, Phys. Rev. D **99**, 103011 (2019).
[108] M. D. Azari, S. Yamada, T. Morinaga, H. Nagakura, S. Furusawa, A. Harada, H. Okawa, W. Iwakami, and K. Sumiyoshi, Phys. Rev. D **101**, 023018 (2020).
[109] C. J. Stapleford, D. J. Väänänen, J. P. Kneller, G. C. McLaughlin, and B. T. Shapiro, Phys. Rev. D **94**, 093007 (2016).
[110] A. Dighe and M. Sen, Phys. Rev. D **97**, 043011 (2018).
[111] R. F. Sawyer, Phys. Rev. Lett. **116**, 081101 (2016).
[112] S. Chakraborty, R. S. Hansen, I. Izaguirre, and G. Raffelt, J. Cosmol. Astropart. Phys. 03 (2016) 042.
[113] S. Abbar and H. Duan, Phys. Rev. D **98**, 043014 (2018).